Sippl, C., Schurr, B., Asch, G., Kummerow, J. (2018): Seismicity Structure of the Northern Chile Forearc From >100,000 Double-Difference Relocated Hypocenters. - *Journal of Geophysical Research*, *123*, 5, pp. 4063—4087.

DOI: http://doi.org/10.1002/2017JB015384

Journal of Geophysical Research: Solid Earth

RESEARCH ARTICLE
10.1002/2017JB015384

Key Points:
- Eight years of IPOC network seismic data were harvested for microseismicity, obtained catalog features 101k events
- Majority of seismicity is at intermediate depths, where a usual double seismic zone grades into a highly active, 25 km thick cluster
- Pervasive upper plate seismicity is observed in an area around 21 degrees S, forming a wedge-like structure extending down to the interface

Supporting Information:
- Supporting Information S1
- Data Set S1
- Data Set S2

Correspondence to:
C. Sippl,
sippl@gfz-potsdam.de

Citation:
Sippl, C., Schurr, B., Asch, G., & Kummerow, J. (2018). Seismicity structure of the northern Chile forearc from >100,000 double-difference relocated hypocenters. *Journal of Geophysical Research Solid Earth*, *123*, 4063–4087. https://doi.org/10.1002/2017JB015384

Received 21 DEC 2017
Accepted 30 MAR 2018
Accepted article online 6 APR 2018
Published online 19 MAY 2018

Seismicity Structure of the Northern Chile Forearc From >100,000 Double-Difference Relocated Hypocenters

C. Sippl[1], B. Schurr[1], G. Asch[1], and J. Kummerow[2]

[1]German Research Centre for Geosciences (GFZ), Potsdam, Germany, [2]Institute of Geological Sciences, Free University of Berlin, Berlin, Germany

Abstract In this study, we present high-resolution seismicity images of the northern Chile subduction zone forearc. We used 8 years of continuous seismic waveform data from the Integrated Plate Boundary Observatory Chile network and auxiliary stations to produce an extensive earthquake catalog containing 101,601 double-difference relocated earthquake hypocenters using automatic event detection and phase picking routines. The minimum magnitude of retrieved events is <2, and the catalog is estimated to be complete at magnitudes above ~2.8. Intraslab seismicity makes up the majority of detected earthquakes. Where the seismogenic zone of the megathrust is active, a clear separation of seismicity into three distinct planes can be observed. The uppermost plane corresponds to the plate interface, which is observed to terminate downdip at a depth of 50–55 km. The other two planes, located ~7 and ~26 km below the slab surface, dip at a constant angle of about 20° until they are absorbed by a 25 km thick highly active cluster of intermediate-depth seismicity at depths of 80–120 km. Downdip of this cluster, the slab steepens and lower plate seismicity is considerably sparser, even absent in the northern part of the study area. Upper plate seismicity is also considerable, with a segment between 21 and 21.6°S standing out for featuring pervasive activity occurring all the way down to the plate interface. Here the seismicity resembles a wedge in west-east profile view and occurs where the upper plate crust is coldest based on thermal models.

1. Introduction

Subduction zone forearcs are the seismically most active regions on Earth, both in terms of seismic moment release and seismicity rate. Earthquakes occur in the upper plate, the subducted (lower) oceanic plate and along the interface between both plates. Wadati-Benioff zone seismicity, that is, earthquakes occurring along dipping planes that trace the subducted slab into the mantle, has been known since before the concepts of plate tectonics and subduction were even established (e.g., Benioff, 1949). At the most shallow level, Wadati-Benioff zone seismicity is dominated by earthquakes along the plate interface, the seismogenic zone of the megathrust fault. This seismicity is intermittent in both time and space, presumably controlled by heterogeneous frictional properties of the megathrust. Locked patches (asperities) can be seismically quiet until they break in large earthquakes, followed by vigorous aftershock series. Creeping or partly locked sections may produce more continuous seismicity (e.g., Holtkamp & Brudzinski, 2014; Lay et al., 2012; Schurr et al., 2012). The lower limit of the seismogenic zone can be controlled by temperature and lithology (e.g., Oleskevich et al., 1999; Scholz, 1998), by transitions of pore pressure and/or permeability (Saffer & Tobin, 2011), or geometrically defined by where the oceanic plate intersects the upper plate Mohorovičić discontinuity and gets into contact with a serpentinized mantle wedge.

Seismicity further downdip occurs within the slab and appears to be less temporally clustered than interface seismicity. In many subduction zones, intraslab seismicity defines two parallel dipping planes that are separated by 25–35 km (Hasegawa et al., 1978; Wang, 2002; Yamasaki & Seno, 2003). The distance between upper and lower plane appears to depend on the thermal state of the slab, with older and colder slabs showing more widely spaced planes (Brudzinski et al., 2007). While upper plane seismicity is often interpreted to occur within the downgoing oceanic crust, the lower seismicity plane is certainly situated inside the oceanic mantle lithosphere. The occurrence of slab earthquakes at intermediate depths (i.e., downdip of the seismogenic zone of the megathrust) has been linked to mineral reactions within the oceanic lithosphere. The breakdown

of hydrous mineral phases releases water, which increases the pore fluid pressure and may enable earthquake occurrence (Hacker, Abers, & Peacock, 2003; Hacker, Peacock, et al., 2003; Kerrick & Connolly, 2001; Kirby, Stein, et al.,1996; Wang, 2002). Whether this mechanism referred to as dehydration embrittlement (Jung et al., 2004; Kirby, Stein, et al., 1996) is driving the earthquakes, or whether some form of strain localization and shear heating (e.g., John et al., 2009; Kelemen & Hirth, 2007) generates them, is still under debate. Hacker, Peacock, et al. (2003) have shown that slab seismicity appears to correlate with where dehydration reactions are predicted to occur from phase diagrams and the thermal structure of the slab. Since slab composition does not dramatically vary between different subduction zones, the thermal state of downgoing slabs (see, e.g., Syracuse et al., 2010) mainly controls depth extent, intensity, and geometry of slab seismicity and thus is also responsible for differences in the water budget of the lithosphere (Van Keken et al., 2011). The water released into the mantle wedge through metamorphic dehydration reactions in the slab is thought to induce melting that is responsible for arc magmatism (e.g., Tatsumi, 1986). Lower plane seismicity has been associated with antigorite breakdown within serpentinized oceanic mantle lithosphere (Peacock, 2001; Rüpke et al., 2004; Yamasaki & Seno, 2003), which requires significant hydration of the oceanic mantle either at the mid-oceanic ridge or through bend faulting at the outer rise (e.g., Ranero et al., 2003). With antigorite being stable up to ~650°C (e.g., Plümper et al., 2016; Rüpke et al., 2004), lower plane seismicity may trace this isotherm. It is currently unclear whether the upper plane of double seismic zones is situated inside the oceanic crust or in the uppermost oceanic mantle. Hacker, Peacock, et al. (2003) proposed a crustal origin of the upper plane and associated it with lawsonite breakdown during eclogitization of basaltic crust, a reaction that has been shown to be seismogenic in laboratory experiments (Okazaki & Hirth, 2016).

Many subduction zone forearcs also exhibit seismicity inside the upper plate, which can be diffuse or localized on upper plate fault systems. Splay faults have been shown to cut through the upper plate to the plate interface and have been identified in the offshore as well as the onshore part of the forearc portion of the upper plate (e.g., Melnick et al., 2012; Park et al., 2002). In oblique subduction settings, strain partitioning between purely convergent motion on the plate interface and trench-parallel sliver motion (Jarrard, 1986) further inside the upper plate frequently gives rise to strike-slip fault systems in the forearc basin or even further inland (e.g., Nocquet et al., 2014). Moreover, seismicity cross sections through active subduction zones frequently show diffuse upper plate seismicity located above the plate interface (e.g., Bloch et al., 2014; Reyners et al., 2011; Yamasaki & Seno, 2003) that can not be attributed to one of the processes described above but likely represents bulk deformation of the upper plate.

In this study, we analyze 8 years of seismicity in the northern Chile subduction zone, based on continuous recordings acquired in the framework of Integrated Plate Boundary Observatory Chile (IPOC; http://www.ipoc-network.org/). We present a regional earthquake catalog containing more than 100,000 double-difference relocated earthquakes with magnitudes down to two, comprehensively mapping upper and interplate deformation and outlining structures within the downgoing Nazca plate in unprecedented detail. We use the obtained seismicity distribution to check existing models of intermediate-depth slab seismogenesis by comparing our high-resolution locations to structural evidence from receiver function images, thereby evaluating the origin of these earthquakes. Moreover, we discuss along-strike variation and specific structures identified in the earthquake catalog and attempt to explain their cause.

2. Regional Setting

In northern Chile, the Nazca plate subducts beneath the South American Plate with a velocity of 68 mm/year in a direction N76°E (Angermann et al., 1999; Norabuena et al., 1998). Situated between two regions of flat slab subduction, the Pampean flat slab further south (Ramos et al., 2002) and the Peruvian flat slab further north (e.g., Gutscher et al., 1999), the study region exhibits normal subduction at an angle of ~20° in the upper 100 km (e.g., Cahill & Isacks, 1992; Yuan et al., 2000). The along-arc segment between 18.5 and 23.5°S constituted a prominent seismic gap along the South American margin that was last ruptured by a megathrust earthquake in 1877 (Comte & Pardo, 1991; Lomnitz, 2004) and is framed by the rupture areas of the 1995 Antofagasta earthquake (M_w 8.1; e.g., Ruegg et al., 1996) to the south and the 2001 Arequipa earthquake (M_w 8.4; e.g., Perfettini et al., 2005) to the north. Since late 2006, the IPOC program was set up in northern Chile to geodetically and geophysically monitor this seismic gap that was partially closed by the 2014 Iquique earthquake (M_w 8.1; e.g., Hayes et al., 2014; Schurr et al., 2014).

With an age of the incoming Nazca plate at the north Chilean trench of ~46 Ma (Van Keken et al., 2011), the northern Chile subduction zone has a thermal parameter ϕ, which is the product of plate age and its vertical descent rate (Kirby et al., 1991), of ~1,780 km (Syracuse & Abers, 2006), which implies it is an intermediate subduction zone in terms of thermal structure (Springer, 1999; Wada & Wang, 2009). Intermediate-depth seismicity in northern Chile has been shown to form a double seismic zone by various authors (Bloch et al., 2014; Brudzinski et al., 2007; Comte et al., 1999; Dorbath et al., 2008; Rietbrock & Waldhauser, 2004), but estimates of the spacing between the two planes vary between 9 (Rietbrock & Waldhauser, 2004) and ~25 km (Comte et al., 1999). The Moho of the downgoing plate has been imaged with several receiver function studies based on different seismic data sets (e.g., Sodoudi et al., 2011; Wölbern et al., 2009; Yuan et al., 2000) and has been shown to vanish at a depth of about 100 km, which hints at the completion of oceanic crust eclogitization at this depth (see section 7.2).

3. Data

We used recordings from the IPOC seismic network (GFZ & CNRS-INSU, 2006) as well as auxiliary permanent or temporary stations (see Figure 1) that were deployed in the years 2007–2014 between roughly 19 and 24°S. While we exploited all available data from the permanent IPOC seismic stations as well as permanent stations from the CSN (Centro Sismológico Nacional) and GEOFON (GEOFON Data Center, 1993), we only added selected stations from the different temporary deployments inside the analyzed time span (see Figure 1). These temporary deployments include the WestFissure (Wigger et al., 2016) network operated by the Free University of Berlin, and the MINAS (Asch et al., 2011) and IQ networks operated by GFZ Potsdam.

The reasoning for not including all available temporary stations is that we aimed to obtain an earthquake catalog that is as homogeneous in time as reasonably possible, that is, has a temporally constant distribution of completeness magnitude. Such a catalog then also allows for the investigation of temporal changes and/or trends in seismicity rate.

4. Retrieval of the Seismicity Catalog

Previous studies of subduction zone seismicity structure have either relied on global earthquake catalogs (e.g., Brudzinski et al., 2007; Syracuse & Abers, 2006), usually the EHB catalog (Engdahl et al., 1998), or made use of data from local temporary deployments (Abers et al., 2006; Hasegawa et al., 1978; Protti et al., 1994; Rietbrock & Waldhauser, 2004). The main disadvantage of global catalogs is that they only contain events with relatively large magnitudes (typically above M~4.5) and that their location uncertainties are higher. Local catalogs, on the other hand, generally only cover a short period of time (typically ~2 years), are often spatially limited and incomplete in seismically highly active areas, because manual picking is performed mainly to gain a good (i.e., well distributed) set of travel times for tomography. In regions that have had long-term coverage by a reasonably dense seismic array, a situation that usually leads to quantities of data that are beyond what can be manually picked, automatized event detection and location approaches have the potential to produce an earthquake catalog that is both homogeneous (i.e., complete down to a certain magnitude) and has high resolution over an extended period of time. However, most large high-quality earthquake catalogs from subduction zones, for example, from Japan (JMA catalog, e.g., Igarashi et al., 2001; Yano et al., 2017) or New Zealand (GeoNet catalog, e.g., Reyners et al., 2011), still come from national agencies that have devoted manpower to manual phase picking over a long period of time. Examples of automatically obtained large earthquake catalogs are currently still few (e.g., Lange et al., 2012; Sippl et al., 2013).

In this study, we applied a modified version of the processing chain described in Sippl et al. (2013) to eight years of continuous waveform data from the aforementioned station network. This processing chain consists of a recursive short-term average over long-term average (STA/LTA) trigger (Withers et al., 1998) with adaptive threshold, an event association routine based on the calculation of travel time grids, as well as the use of dedicated P (Aldersons, 2004; Di Stefano et al., 2006) and S phase pickers (Diehl et al., 2009). Between the single steps, the event location is updated and spurious picks are removed. The reader is referred to Sippl et al. (2013) for a more detailed description of the automatic event detection and phase picking process. For the stages of event detection and the (re)picking of phases, we used the 1-D velocity model of Graeber and Asch (1999) and required a minimum of eight constituent phase picks for each event. For further quality selection, we rejected events that had cumulative pick-weight sums (see Sippl et al., 2013, for details) of less than 30 for P+S and 10 for S alone. Local magnitudes were determined from maximum amplitudes on the horizontal

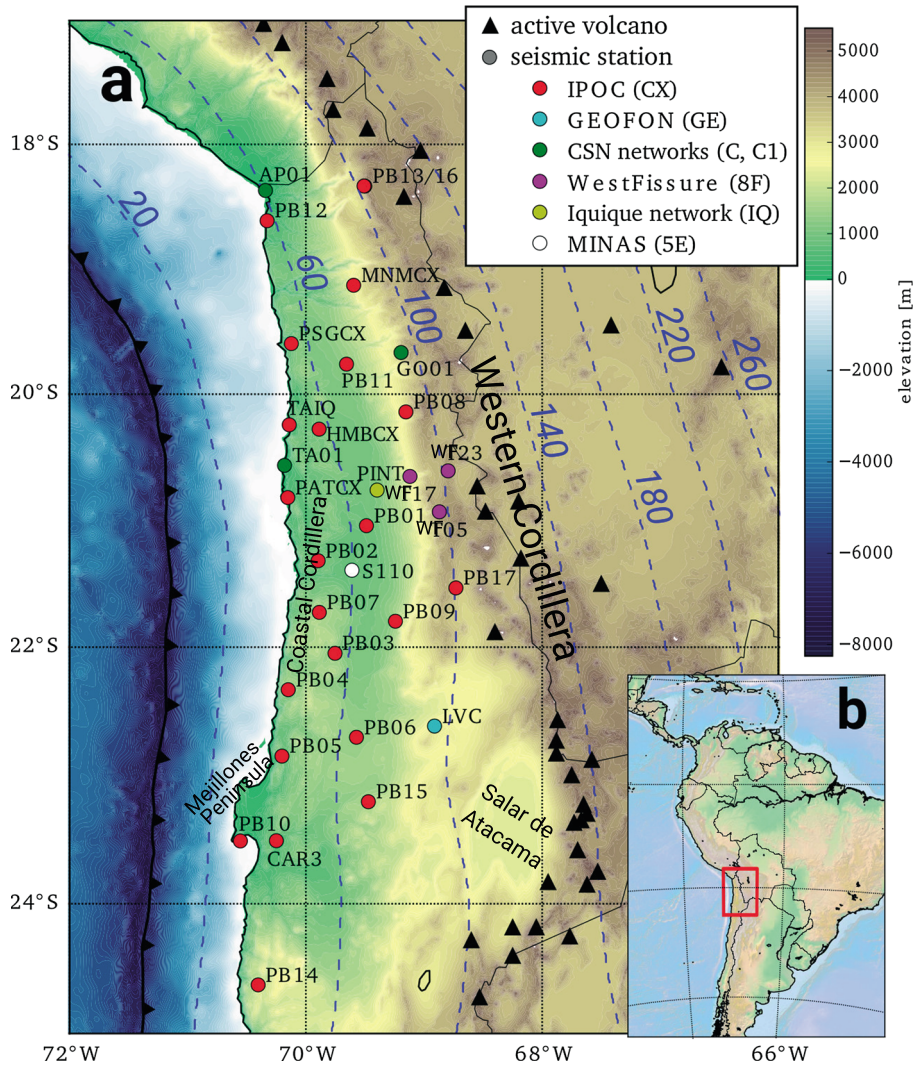

Figure 1. (a) Topographic and bathymetric map of the study area. Seismic stations used in this study are shown as circles, with the circle color indicating the network as listed in the legend. Black triangles denote the locations of active volcanic centers as listed in the National Oceanic and Atmospheric Administration volcano database (https://www.ngdc.noaa.gov/nndc/struts/form?t=102557&s=5&d=5). The solid black barbed line marks the trench, dashed blue lines are depth isolines of the Nazca slab surface beneath the study area, after slab model SLAB1.0 (Hayes et al., 2012). Subfigure (b) shows the location of the map in (a), indicated with a red frame.

components after Hutton and Boore (1987). We retrieved a total of 1,200,404 P and 688,904 S phase picks with average uncertainties of 0.11 and 0.37 s, respectively (see Table S1 in the supporting information).

The identified and picked events were then jointly relocated using Velest (Kissling et al., 1994), keeping the velocity model fixed to the 1-D model of Graeber and Asch (1999). Picks that had residuals deviating from the event's mean residual by more than 2 standard deviations and had an absolute residual of >2 s were removed. To account for the geometry of the high-velocity slab as well as the difference between oceanic and continental crust in the study region, we used a subset of 3,886 events between 20.5 and 23°S to calculate an E-W oriented 2-D velocity model with the tomography code simul2000 (Evans et al., 1994; Thurber, 1983). The final 2D v_p model (v_p/v_s was kept fixed to the values from the 1-D model), obtained by adjusting the damping using L-curve analysis (Eberhart-Phillips, 1986), is provided in Table S2 and plotted in Figure S2 in the supporting information. All events were relocated in this model using simul2000, which had the effect of providing a more realistic slab dip, especially in the offshore updip part of the slab.

In a final relocation step, double-difference relocations (Waldhauser & Ellsworth, 2000) using both catalog and cross correlation derived travel time differences for closely located event pairs were computed for the entire

suite of events. Since relocating >100k events in a single run of hypoDD proved to be impossible due to memory constraints, we subdivided the study area into 11 overlapping E-W oriented swaths, for which we performed the double-difference relocations separately. In the 11 separate runs, a total of 19.64 million catalog P and 7.63 million catalog S travel time differences were used, as well as 7.27 million P cross-correlation lag times and 1.70 million S cross-correlation lag times. About 70% of all earthquakes were situated in the overlapping segments and were thus relocated twice. For these events, we used the average between both locations as the final location, and their separation as a quality check (see Figure S1). For the final catalog, we only retained events that were situated in clusters of >100 earthquakes. Since such events had to be isolated from all neighboring earthquakes by >15 km, which is a rarity inside a dense catalog of >100k events, this restriction mainly served to remove events far outside the station network as well as individual mislocations.

5. Estimating Location Errors

Acquiring a realistic estimate of hypocentral location uncertainties is not a simple, straightforward task. Formal errors given by many standard single-event location tools have been shown to significantly underestimate true location error (e.g., Pavlis, 1986). Many authors that use double-difference relocations estimate location errors from the sharpness of obtained structures or with a bootstrap procedure. As mentioned by Waldhauser and Ellsworth (2000), one has to be aware that these error estimates, which are commonly rather small, are only relative errors; that is, they quantify the uncertainty in relative positioning of events within a cluster but give no indication about the uncertainty of the entire cluster's position in space.

To estimate absolute location error, we relocated our entire earthquake catalog with the probabilistic routine NonLinLoc (Lomax et al., 2000), using the 1-D model of Graeber and Asch (1999). The resulting distribution of location error estimates, that is, the size of the ellipsoids that contain 68% of the output probability density function, is shown in Figure 2. We subdivided the study region into squares of 0.25° × 0.25° and three depth levels and averaged the size of the error ellipsoids in X, Y, and Z directions for all events within each of these grid cells. Cells that contained less than 20 events are left blank. This plot mainly visualizes location error as a consequence of pick accuracy and event-station geometry, whereas the effect of velocity model inadequacy is not fully taken account of. We see that absolute location errors inside the network are typically small (<5 km) but increase outside the network's footprint toward east and west. Hypocentral depth errors appear to be systematically larger than horizontal location errors, although this effect is small inside the network.

From the sharpness of imaged features in cross section (Figure 6), we can estimate that relative location errors for events inside the seismic network should not exceed 1–2 km. Offshore earthquakes to the NW of the network show considerable scatter (Figure 6, profiles A-A′ to C-C′), which indicates that depth resolution this far offshore is breaking down.

6. Results

A summary plot of all 101,601 earthquakes, in map view as well as projections onto a longitudinal and a latitudinal plane, is shown in Figure 3. The most prominent feature of the map view plot is the N-S striking band of intermediate-depth seismicity (hypocentral depths between 80 and 140 km) that is present along the entire area that we resolve (see Figure 2). Activity inside this band makes up ∼60% of the total number of earthquakes in our catalog (Figure 3). At 21°S, this band shows a kink or offset, with events to the south occurring further east than to the north of it. We will examine the nature of this offset more closely in section 6.3.2. Seismicity downdip (and hence east) of the highly active band at intermediate depths is absent north of the offset, whereas a number of deeper clusters occur down to 250 km depth south of it. These clusters lie outside our seismic network, where our event detection capability is reduced and hence the catalog is incomplete. However, the change in seismicity style along the slab, from the active band to isolated seismogenic areas, should be robust. Further updip, seismicity is likewise less dense but present. Earthquakes only extend all the way to the trench in the northern part of the study area, whereas they terminate ∼50 km east of the trench south of 20.8°S. The magnitude distribution of the earthquake catalog is shown in Figure S3: the majority of earthquakes has magnitudes between 2 and 3; the completeness magnitude of the catalog is estimated to lie between 2.7 and 2.9.

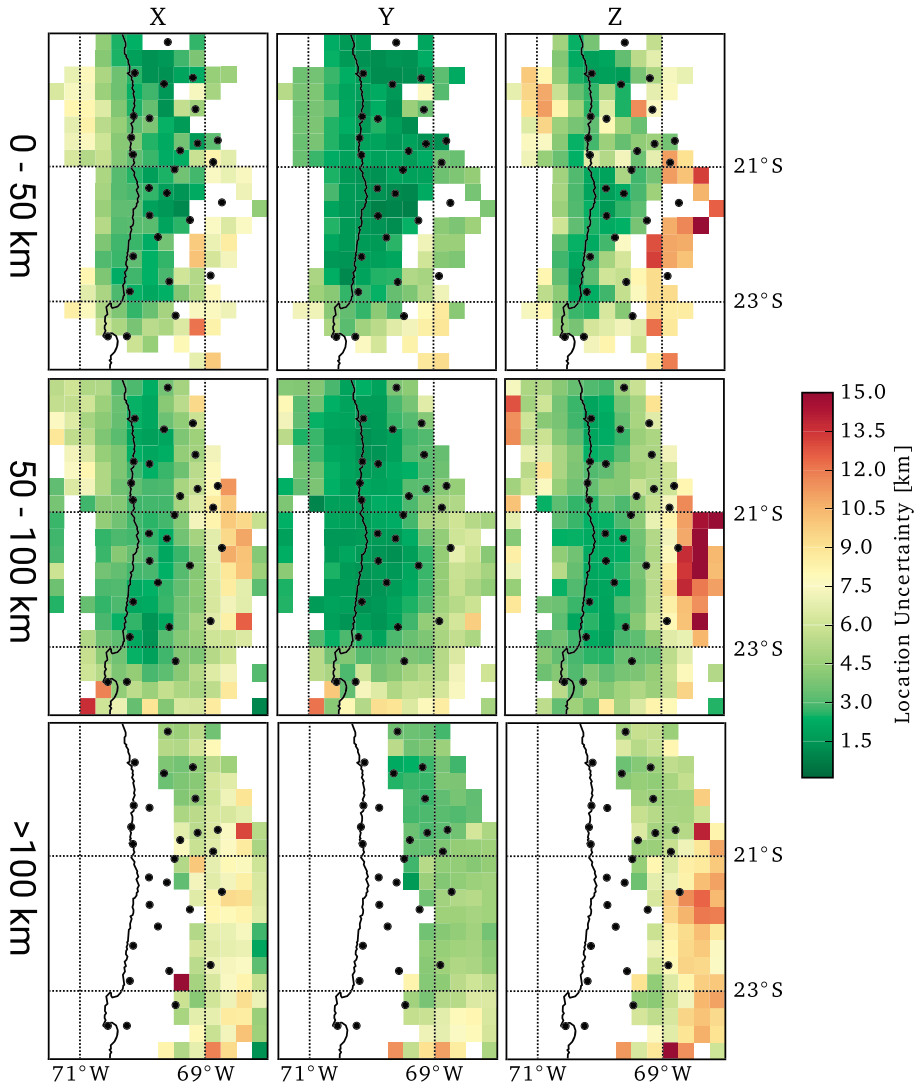

Figure 2. Location uncertainties determined with NonLinLoc, shown for three different depth levels and *X*, *Y*, and *Z* directions. For each 0.25*0.25° bin, the extent of the error ellipsoids for all earthquakes was averaged to obtain the final plotted value. Bins containing less than 20 events were left blank. Black dots denote the stations of the seismic network.

In the following, we will present a more detailed account of the seismicity distribution in the study area, based mainly on the cross-section plots in Figure 6. We produced a new local slab surface model (section 6.1) and classified events based on their distance from it. In sections 6.2 and 6.3, we discuss the main features in the seismicity distribution, going from top to bottom.

6.1. Slab Model and Event Categorization

We plotted narrow west-east seismicity cross sections of 10 km half width every 0.1° of latitude, on which we handpicked the slab surface at 37 to 121 points per cross section. Where interplate seismicity occurs, that is, along the seismogenic zone from the trench to a depth of ~55 km, we set the picks in the center of the interface seismicity. Beyond the downdip termination of interface seismicity we tried to extrapolate the interface by staying above the second plane of seismicity and at the same time smoothly connecting it with the top of the intermediate-depth cluster further downdip. A surface defined by a fourth-order polynomial was then fitted to all 2,954 handpicked points using a least squares approach; the plane is shown in 2-D and 3-D view in Figure 4, and the misfit values for all individual points are shown in Figure S4. Figure 4 shows a transition from a steeper slab with a constant dip angle in the north to a slab with a terrace-like feature, that is, a region with very shallow dip at 80- to 100-km depth, followed by a steeper dip further downdip, in the south.

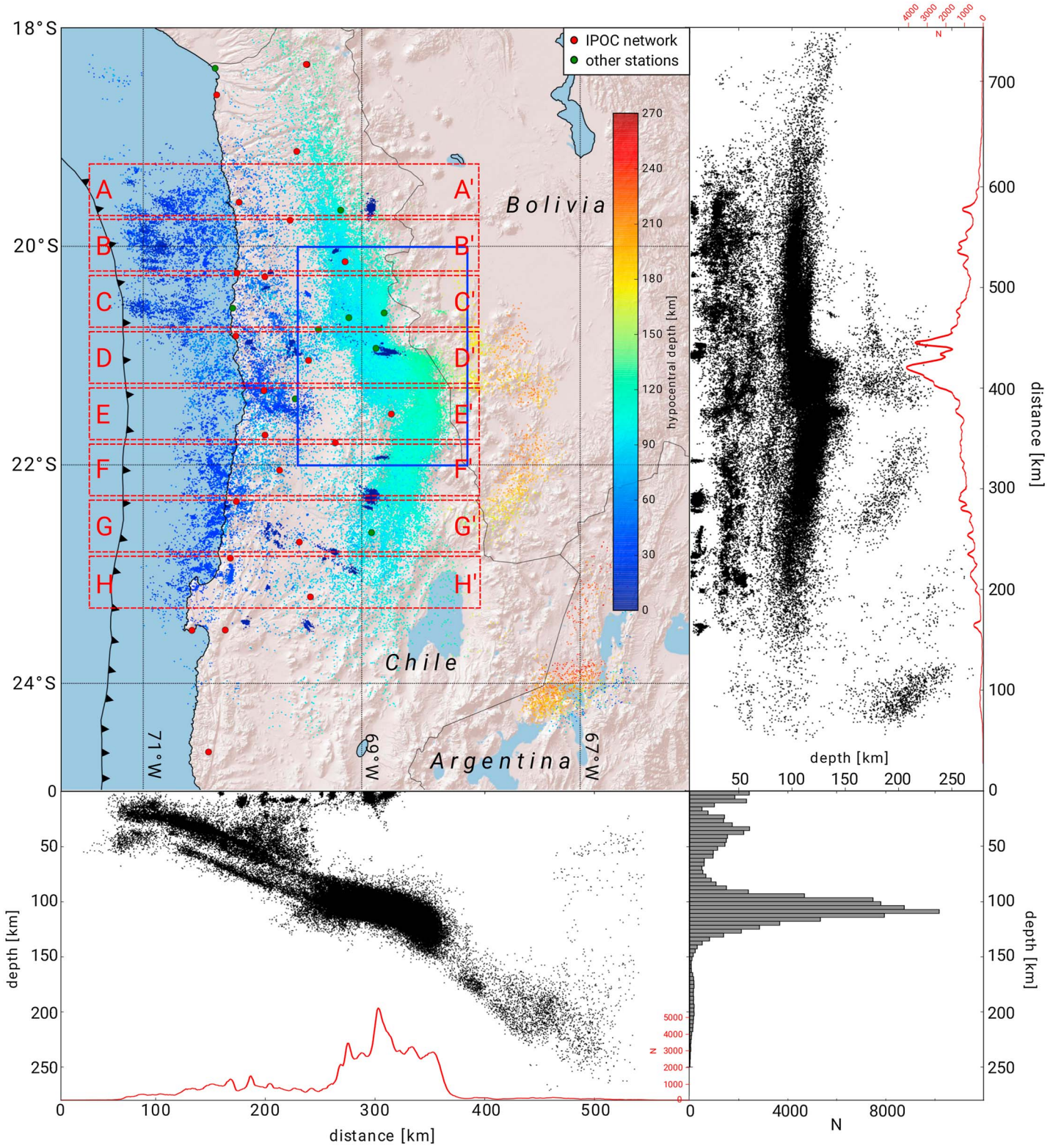

Figure 3. All 101,601 earthquakes detected and located in this study, plotted in map view as well as projected onto a single longitudinal (below) and latitudinal (right) plane. In the map view plot, events are color coded by their hypocentral depth and plotted on top of a shaded relief map. Red and green circles depict the seismic network stations that were used for catalog production. In the cross sections, the red line at the base depicts a moving-window event sum. Every kilometer along the profile, the total number of earthquakes within a 5 km-wide corridor centered on that present location was determined. In the bottom right plot, the distribution of hypocentral depths in the data set is displayed. Red dashed boxes in the map view plot show the location of the profiles displayed in Figure 6, the solid blue box marks the extent of the zoomed-in map view plot in Figure 9.

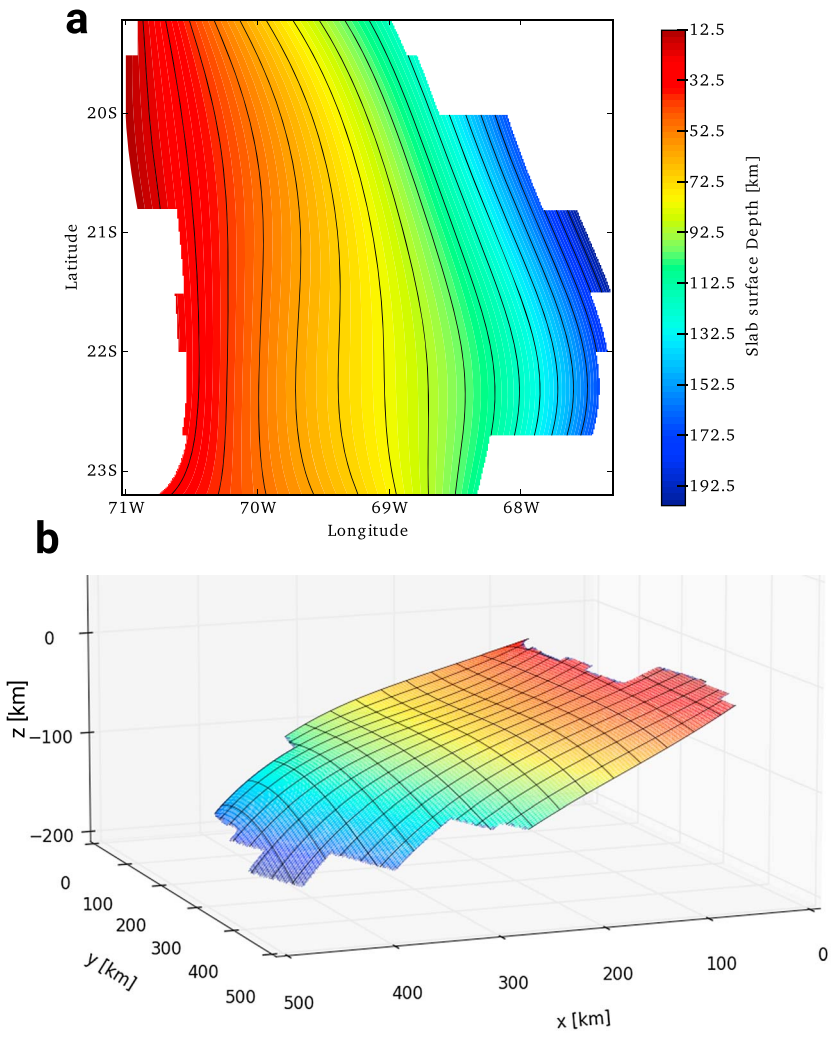

Figure 4. Plots of the slab surface determined in this study in top view (a) and as 3-D view, seen from the north. For an image of the datapoints that were used to acquire this interpolation, refer to Figure S4.

Table 1
Description of the Spatial Classification Scheme Applied to All Earthquakes of the IPOC Catalog

Class name	Meaning	Color	Areas S of 21°S	Areas N of 21°S
NN	Not classified	Black	Events S of 23.6°S	Events N of 19°S
			events E of 68°W	events E of 68°W
			W of 70.8°W and >10 km below slab top (ST)	W of 70.8°W and >10 km below ST
ID	Intermediate-depth cluster	Cyan	69.1°W–68°W and ±30 km from ST	69.6°W–68°W and ±30 km from ST
UP	Upper plate	Magenta	70.8°W–69.1°W and >3 km above ST	70.8°W–69.6°W and >3 km above ST
			69.1°W–68°W and >30 km above ST	69.6°W–68°W and >30 km above ST
P1	Plate interface	Blue	70.8°W–69.1°W and ±3 km around ST	70.8°W–69.6°W and ±3 km around ST
			W of 70.8°W and ±10 km around ST	W of 70.8°W and ±10 km around ST
P2	Upper plane	Green	70.8°W–69.1°W and 3–16 km below ST	70.8°W–69.6°W and 3–16 km below ST
P3	Lower plane	Red	70.8°W–69.1°W and >16 km below ST	70.8°W–69.6°W and >16 km below ST

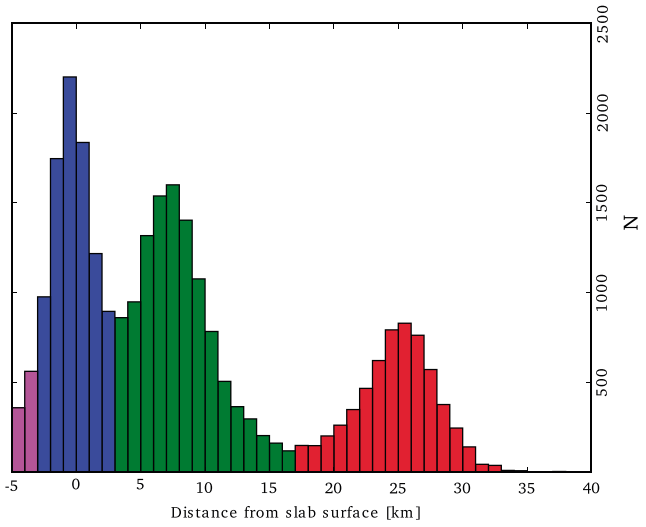

Figure 5. Histogram of earthquake occurrence depending on distance from the slab surface, as defined with the fitted plane of Figure 4. It is apparent that the distribution shows three maxima: one around 0 km, which can be identified with seismicity along the plate interface, a second one between 6 and 8 km below the slab surface, and a third maximum 25–27 km below the slab surface. We subdivided updip slab seismicity into three classes based on this histogram plot, here indicated by the coloring. Events more than 3 km above the slab surface were labeled "upper plate events" (magenta).

The distribution of misfits (Figure S4) shows that although a relatively high-order polynomial was chosen, true short-wavelength slab curvature is still underestimated by this parameterization in some areas.

We spatially divide the seismicity into six compartments or classes based on the scheme outlined in Table 1. We first separate the strong intermediate-depth strike-parallel cluster east of a north-south line, which is offset at 21°S (see section 6.3). The depth distribution of earthquakes with respect to the slab surface west of this line (Figure 5) shows three maxima corresponding to three vertically distinct bands of seismicity associated with the downgoing slab updip of the intermediate-depth cluster: plate interface, upper band, and lower band (see Table 1 and Figure 5). The downdip end of the interface seismicity can not always be perfectly separated from upper plate seismicity and hence shows some blur. The earthquakes far offshore in the northern part of the study area (Figure 3) are mostly foreshocks and aftershocks of the Iquique megathrust earthquake in 2014. Their location and particularly depth is less precise due to the one-sided event-station geometry (see Figure 2). We assumed for simplicity that these events are located on the plate interface and hence relaxed the criterion for a plate interface classification west of 70.8°W (see Table 1).

6.2. Upper Plate Seismicity

Upper plate seismicity forms a number of tight clusters at shallow depths, as well as some deeper structures between ~20.5 and ~ 21.5°S (Figure 7a). We found that nearly all of the shallow crustal clusters coincide with open-pit mines. To test whether these events are indeed mining blasts, we evaluated at what time of the day (local time) they were recorded. The histogram in Figure 7c shows a constant background rate of upper plate seismicity throughout the day, which is significantly increased between about noon and 9 p.m. local time. We removed all events between 12 and 9 p.m., which we interpreted as the blasting interval of the mines, from our upper plate subcatalog, and plotted it again (Figure 7b). In this second plot, all shallow crustal clusters except the one in the northeast, which appears to have a tectonic origin, have vanished, indicating that they consisted exclusively of mining blasts. It is worth noting that whereas most seismicity clusters corresponding to mining locations in the northern half of our study area are rather tightly confined, several of them appear as E-W or NW-SE elongated streaks in the southern part of the study area (Figure 7b). This is mostly due to less favorable event-station geometry: since several stations in the SE of the study area (see Figure 3) only came online significantly later than the start of the catalog in 2007, these mining locations were outside the station network for part of the observation time. Thus, location uncertainties were larger for these events, and the main direction of horizontal uncertainty was oriented toward or away from the network center. A trade-off of horizontal uncertainty with depth uncertainty occasionally creates the appearance of inclined structures in profile view (see Figure 6).

The structures outlined by the deeper upper plate seismicity between ~20.5 and ~ 21.5°S were not changed by the aforementioned temporal filtering. The imaged concentration of earthquakes terminates abruptly in the south along an E-W striking line. South of about 21.6°S, the upper plate appears to be largely aseismic. To the north, seismicity is less clustered and intense, with a higher proportion of offshore events. This activity is part of the aftershock series of the Iquique earthquake in 2014. East-west cross-sections D-D′ and E-E′ (Figure 6) show that upper plate events in this area form a wedge and reach all the way down to the plate interface. This was already observed by Bloch et al. (2014) who used a local seismic array with a smaller along-strike footprint around 21°S. The western end of this seismicity correlates well with the coastline (Figures 7a and 7b). A north-south cross section through the upper plate seismicity (Figure 7d) reveals an upward curved alignment of hypocenters toward the southern termination of crustal seismicity. When connected to the surface, this structure would surface south of the Rio Lóa, possibly along the Adamito Fault (Mittelstädt et al., 2018), which has been named Aguirre Fault in Allmendinger and González (2010).

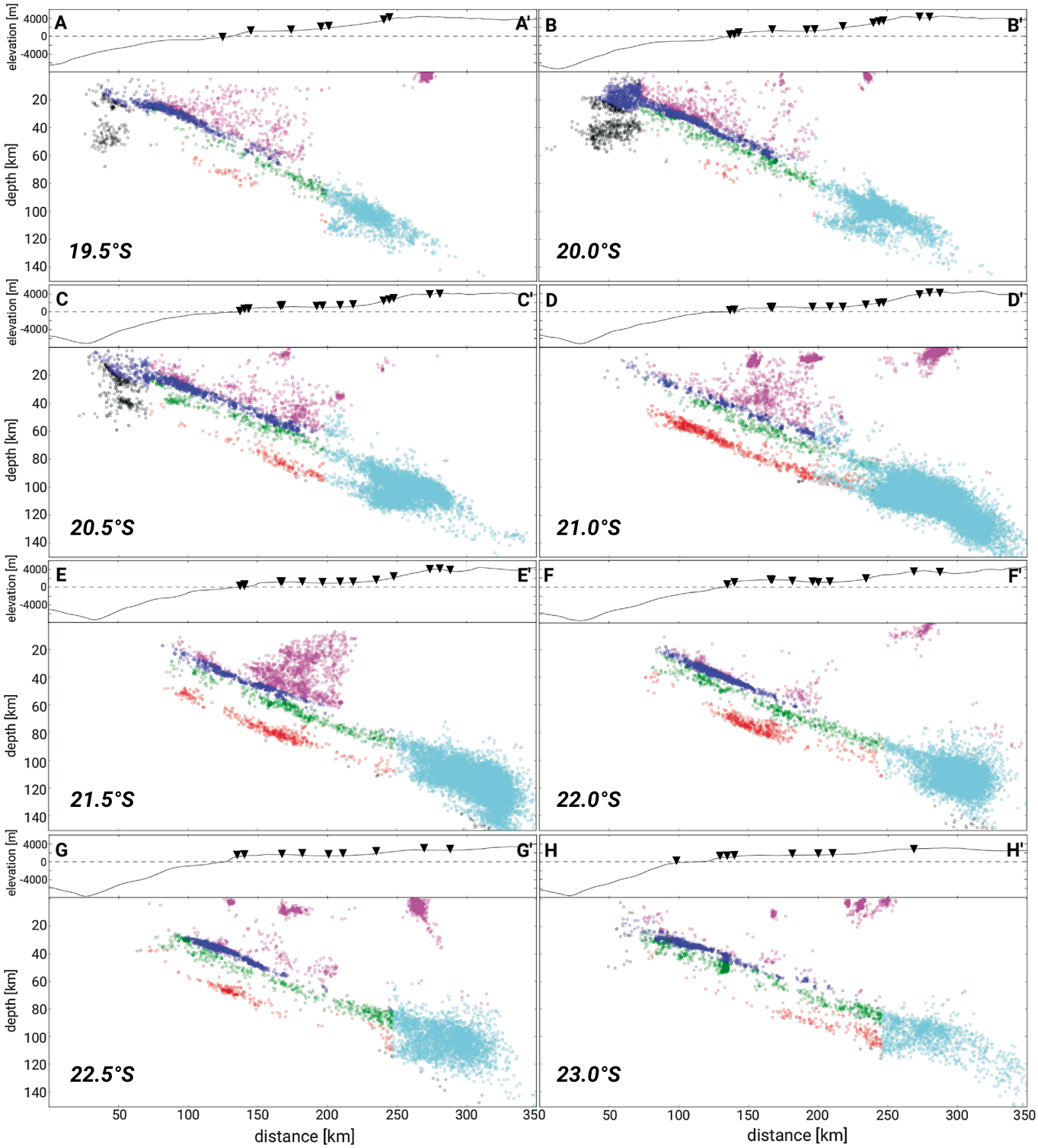

Figure 6. Eight west-east cross sections through the seismically active area, sorted from north to south. Locations of the profiles are displayed in Figure 3. Earthquakes are shown as hollow circles, with circle sizes scaled to their magnitudes, and color according to the classification scheme shown in Figure 5 and Table 1. Additionally, the cluster of intense intermediate-depth seismicity is colored in cyan, and events that do not fall into any of the assigned classes are shown in black. Each profile has a half-width of 25 km around the central latitude displayed in its bottom left corner. Smoothed topography along this swath is shown in the top panels, with the dashed line denoting sea level. Black inverted triangles are the projected locations of stations within 100 km of the profile's central latitude. For profile plots without the color coding, refer to Figure S5 in the supporting information.

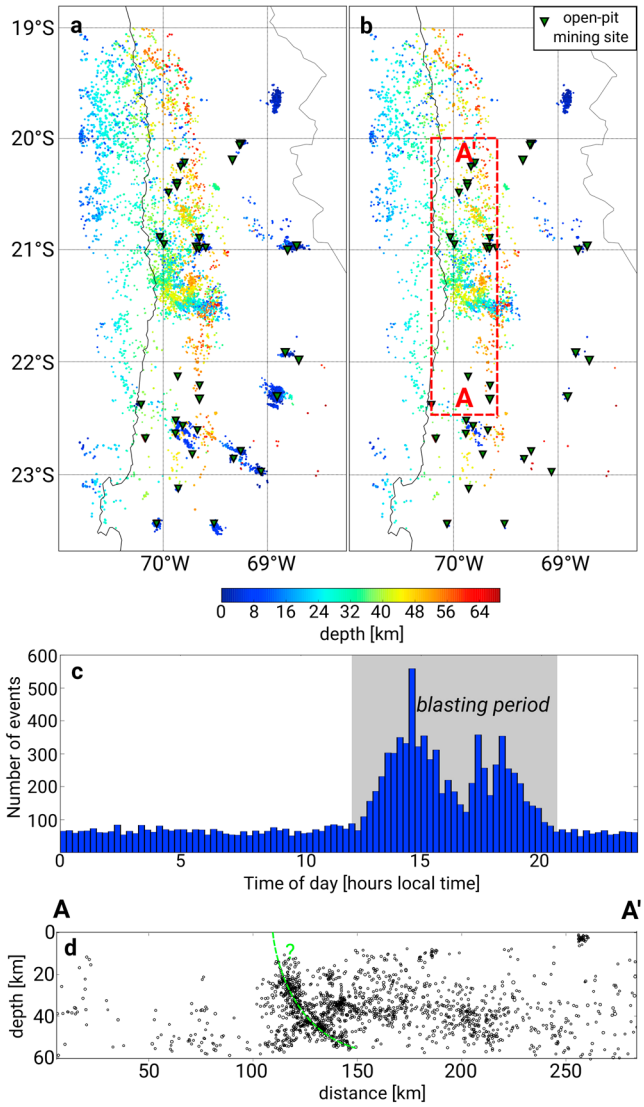

Figure 7. Summary of upper plate events. Subfigure (a) shows a map-view plot of all upper plate events, color coded by hypocentral depths. There is a number of shallow earthquake clusters that correlates, to first order, with known locations of open-pit mines (green inverted triangles). Moreover, deeper upper plate seismicity is observed in a cluster around 20.5 to 21.5°S, and more distributed further north. (b) The same map view plot with events in the "blasting time window" (see subfigure c) removed. All shallow clusters except the one in the northeast have disappeared, which suggests they consisted entirely of mining blasts. (c) Distribution of earthquakes against local time, showing a constant background of tectonic earthquakes occurring at a rate of roughly 60–90 events per bin. Between 12 p.m. and 9 p.m. local time, the event occurrence rate is significantly increased due to blasting activity in the local open-pit mines. Events from this time period were removed in subfigure (b). (d) N-S cross section through the upper plate cluster between 20.5 and 21.5°S. The location of the cross section is indicated in subfigure b. The profile shows an apparent steeply N dipping structure that surfaces around 21.6°S, highlighted in green.

6.3. Slab Seismicity

Slab seismicity can be subdivided into three areas along dip: the area updip of the intermediate-depth cluster, the intermediate-depth cluster itself, and events downdip of this cluster. We will describe the seismicity in this order and also analyze along-strike variations.

6.3.1. Updip Slab Seismicity - Triple Seismic Zone

As already recognized in the categorization histogram (Figure 5), slab seismicity updip of the intermediate-depth earthquake cluster forms three separate bands. This is also evident from the cross sections (Figure 6), where they are colored blue, green, and red. The uppermost band (blue) is seismicity along the plate interface.

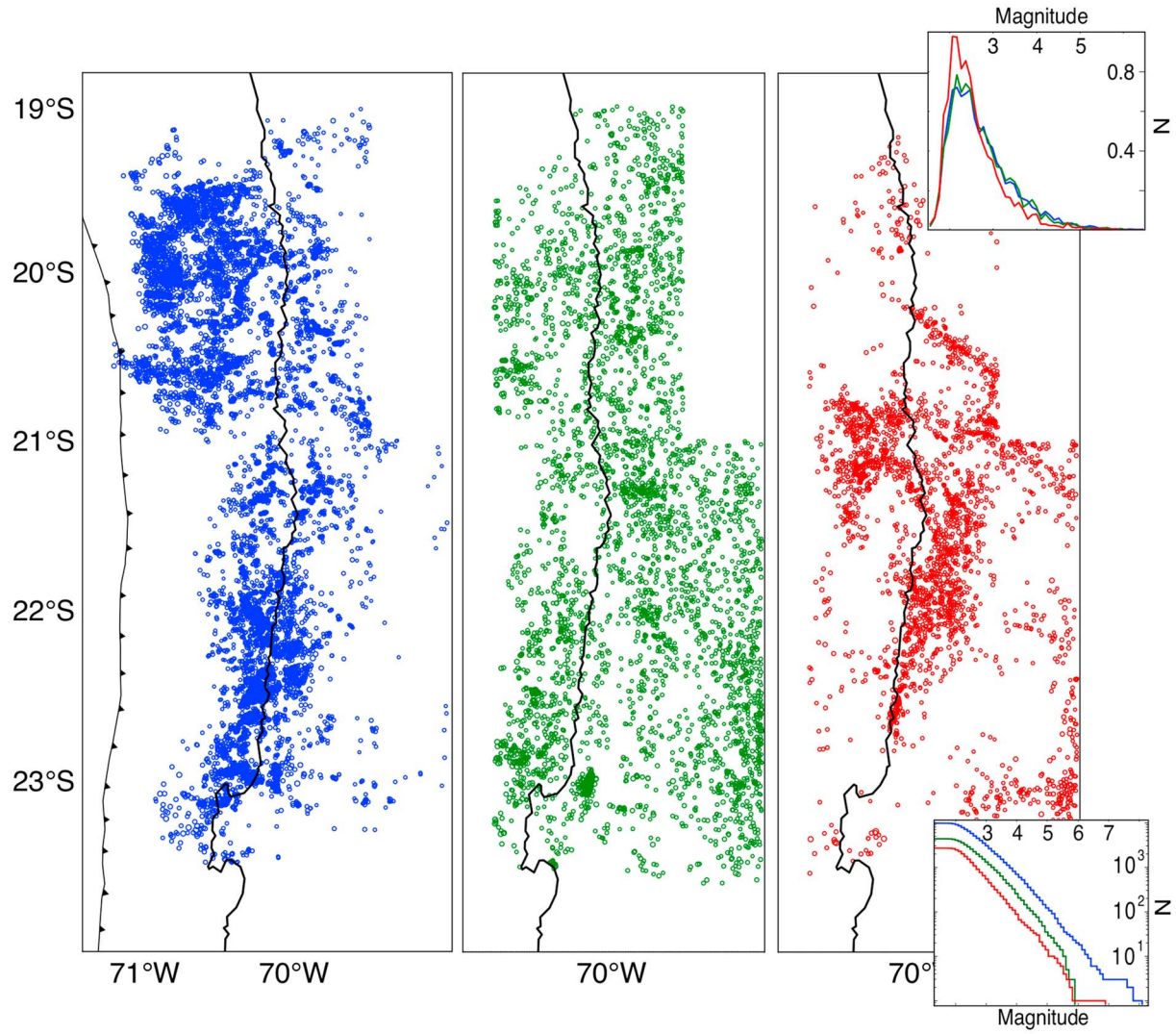

Figure 8. Map view plot of all events in the classes P1 (plate interface; left), P2 (middle plane; center) and P3 (lower plane; right). Note that the left subplot extends further offshore than the other two. It can be seen that P2 events occur very homogeneously, whereas there are clear structures in P1 and P3 event occurrence. Inset on the upper right shows normalized magnitude-frequency distributions for the three seismicity levels (normalization so that the area under each of them is 1). It can be seen that whereas the curves for the interface and upper plane are very similar, the lower plane features a larger proportion of smaller and fewer large events (higher b value). Inset plot on the lower right shows cumulative, logarithmic histograms of the frequency-magnitude distributions for the three event classes.

In most cross sections, especially in the south, it forms a sharp linear structure with an abrupt downdip termination at about 50- to 55-km depth. Updip, it reaches almost to the trench in the northern cross sections (although the location uncertainty far offshore is high—hence the scatter) but terminates at a depth of 20–25 km further south. From the three slab-related seismicity bands, the plate interface has the largest number of earthquakes. Interface activity is clustered in time and space and related to three great megathrust earthquakes (M7.7 2007, M8.1 2014, and M7.6 2014; see Figure S7). There is also some sparse background seismicity on the downdip part of the plate interface (Figure S7). The northern three cross sections (A-A′ to C-C′; Figure 6) cut through the aftershock series of the 2014 Iquique earthquake (Hayes et al., 2014; Schurr et al., 2014), which ruptured the plate interface mostly offshore. Its aftershock series hence also activated the shallow part of the plate interface, which is aseismic throughout the observation period further south (see Figure 3). In the south, the imaged sharp plate interface at deeper depth to large parts corresponds to the aftershock series of the 2007 Tocopilla earthquake (Fuenzalida et al., 2013; Schurr et al., 2012), which ruptured only the deeper part of the interface (see profiles F-F′ to H-H′; Figure 6). The profiles that are located

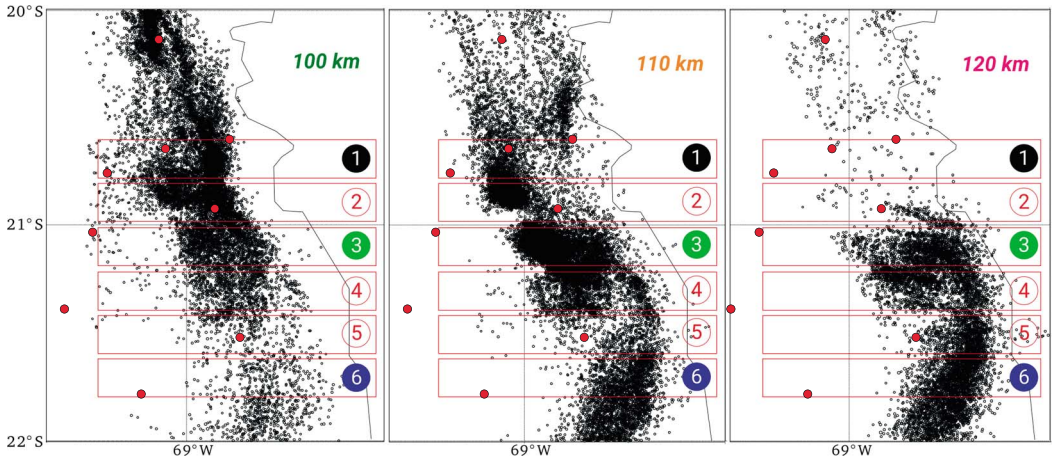

Figure 9. Zoomed-in depth sections at 100, 110, and 120 km of the offset in the intermediate-depth earthquakes. The shown region is marked with a blue frame in Figure 3. The color of the depth labels correspond to the coloring of the depth isolines in Figure 10b. Red frames outline the locations of the profiles in Figure 10, and red dots are seismic station locations.

between the two aftershock series (D-D′ and E-E′; Figure 6) show a less well defined plate interface, most likely due to the smaller number of earthquakes that have occurred on it, and the presence of upper plate seismicity directly above.

About 6–8 km below the plate interface, a second plane of seismicity in the slab is observed throughout the study area. This plane continues downdip beyond the termination of the plate interface seismogenic zone and extends to a depth of 80–90 km, where it merges into the highly active cluster at intermediate depths. Updip, this seismicity band begins at about the same longitude as the plate interface seismicity in the southern cross sections (Figure 6), whereas it does not appear to extend as far updip in the three northern cross sections.

A third seismicity plane is clearly seen 25–27 km below the slab top; its seismicity is colored red in the cross sections in Figure 6. This plane parallels the above planes but is decidedly more variable in its appearance. It is clearest and most continuous in the center cross-sections D-D′ and E-E′, where it extends from directly beneath the updip termination of interface seismicity to the intermediate-depth cluster below. It is nearly absent, however, in the northernmost cross sections (A-A′ to C-C′), and only short segments are active in the south (F-F′ to H-H′). This pattern is also clear from the map view projections in Figure 8, where the deepest plane is more discontinuous and clustered compared to the plate interface and upper plane. The deeper cluster of earthquakes that is imaged in the far offshore portion of cross-sections A-A′ to C-C′ (Figure 6) does most likely not belong to the lower plane but consists of a population of mislocated Iquique aftershocks. Lower plane earthquakes appear to exhibit a different frequency-size distribution than the two upper planes, with a larger number of small earthquakes relative to larger ones (i.e., higher b value). However, this needs to be evaluated with more rigor before any conclusions about mechanisms or driving processes may be made.

6.3.2. Highly Active Seismicity Band at Intermediate Depths

At a depth of 80–90 km, the space between the upper and lower intraslab seismicity planes (green and red) abruptly becomes seismically active, creating a vigorous cluster of seismicity that is 20–25 km thick. The shape of this active region varies along strike. It abruptly terminates along a horizontal edge at about 110-km depth north of 21°S (Figure 6, sections A-A′ to C-C′). Seismicity extends to greater depth south of this latitude, which leads to a clear offset in map view (Figure 3). The nature of this offset is explored in greater detail in Figures 9 and 10. Earlier studies explained the seismicity offset in map view with a slab tear (Rietbrock et al., 2008). However, the dip angle of the slab is constant across the offset, which is rather caused by a downdip (and thus eastward) shift of intraslab seismicity south of ~ 21.6°S compared to north of 21°S. The slab segment between these two latitudes is seismically active at both depth levels and shows a clear kink in slab dip toward deeper depths (Figure 10). Such a kink is also inferred south of section D-D′, albeit with a higher uncertainty because it comes from connecting intermediate-depth seismicity with earthquake locations from the deeper clusters (see below). For cross-sections A-A′ to C-C′, we do not find any seismicity at depths below about 110 km; thus, we can not state whether a slab kink is present. A downdip change in slab dip angle at intermediate depths

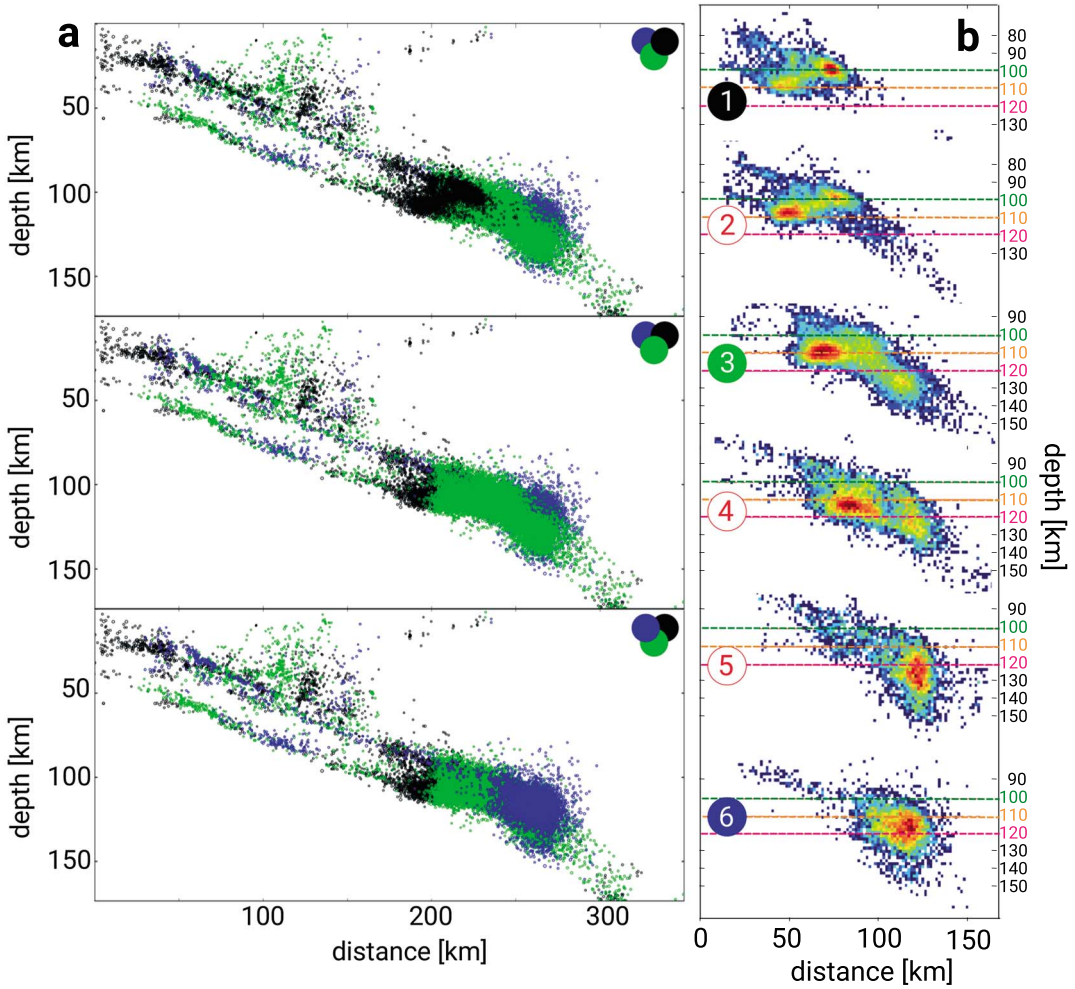

Figure 10. (a) Overlay of three west-east profiles, displayed with the northernmost (upper panel), middle one (center panel), and southernmost (bottom panel) profile on top. The locations of these profiles are depicted in Figure 9 (coloring of the numbers; Figures 1, 3, and 6 correspond to black, green, and blue color). The symbol on the upper right of each plot indicates the plotting sequence of event colors, that is, which color of events is plotted on the bottom, in the middle and on top. (b) Six west-east profiles through the intermediate-depth cluster (locations are shown in Figure 9). Shown are seismicity densities, that is, logarithmically color-coded event numbers for 1× 1 km pixels. The colored dashed lines correspond to the depth levels shown in Figure 9.

has already been observed in earlier studies (Garth & Rietbrock, 2017; Graeber & Asch, 1999; Schurr et al., 2006), but the nature of the map view offset at 21°S is revealed here in detail for the first time.

Figure 3 (right subfigure, red line) shows that the seismicity rate inside the cluster increases along strike from both sides toward the offset at 21°S, whereas the rate is lowered directly at the offset. Event density plots along profiles A-A′ to H-H′ (Figure S6) show that although some internal structure is present within the event cluster, earthquakes do not preferentially align along the continuation of the ingoing two seismicity planes.

6.3.3. Below - Isolated Clusters

Below the downdip termination of intense intermediate-depth seismicity, a number of deeper clusters at depths between 150 and 250 km are present in the catalog at latitudes south of ~21°S. Due to the location of these clusters to the south and east of the seismic network, the number of earthquakes in them is expected to be underestimated, and location accuracy is low (Figure 2). However, the identified clusters in map view (Figure 3) resemble those found in earlier studies with seismic networks located further east (e.g., Schurr et al., 1999). In cross section, we see more scatter in the earthquake locations due to the large azimuthal gap between events and stations, but cross-section D-D′ (Figure 6) shows a continuous planar seismicity structure at larger depths, continuing downward at the "post-kink" dip angle of the intermediate-depth seismicity.

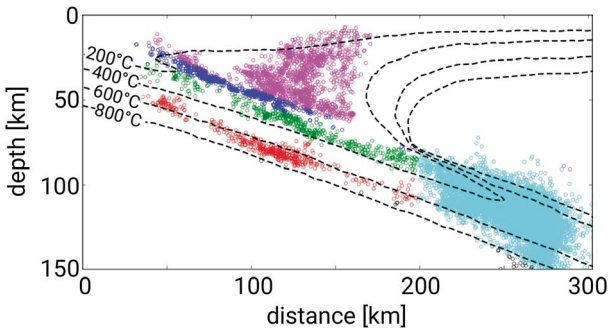

Figure 11. Isotherms from the thermal model of Wada and Wang (2009) overlain onto the seismicity profile at 21.5°S (profile E-E′ in Figure 6). Color coding of seismicity as in Figure 6.

7. Discussion

7.1. Upper Plate Seismicity Correlates With Interplate Locking

The northern Chile forearc upper plate is mostly seismically quiet in global earthquake catalogs. This is despite the fact that its crust exhibits significant faulting (e.g., Allmendinger & González, 2010), including the large-scale strike-parallel Atacama fault system, which cuts through the Coastal Cordillera (e.g., Scheuber & Andriessen, 1990) and is thought to be active and capable of producing large earthquakes (González et al., 2006). This changes dramatically when considering microseismicity recorded by the IPOC network (Figure 7). Our images show that the entire crust is seismically active along a swath which approximately follows the Coastal Cordillera. The activity varies significantly along strike and is highest between ~21 and 21.5° and vanishes almost completely further south. The obtained upper plate seismicity is mostly diffuse but in some places collapses to well-defined planes when projected onto cross sections (Figure 7d).

The wedge-like geometry in west-east cross-section view (Figure 6, section E-E') appears to correlate with the thermal structure of the forearc (Figure 11). Isotherms of the model of Wada and Wang (2009) engulf the seismicity and upper plate seismicity exclusively occurs in areas where temperature does not exceed about 350–400 °C (see Figure 11), approximately the temperature at which quartz becomes ductile. The continuous subduction of the cold oceanic plate beneath cools the upper plate sufficiently so that crustal seismicity can occur down to depths exceeding ~50 km. Figure 12 shows that the area of most intense upper plate seismicity is situated where interplate coupling is low (model from Li et al., 2015; Moreno et al., 2016), between two highs in interplate coupling that correspond to the along-strike extent of rupture during the 2007 Tocopilla and 2014 Iquique earthquake sequences. This along-strike locking low has already been noted by Métois et al. (2013), who proposed this to act as a barrier segmenting the plate interface. However, in their study the locking low is placed 30–40 km further north, into the area that later ruptured in the Iquique earthquake sequence (e.g., Cesca et al., 2016; Hayes et al., 2014; Schurr et al., 2014). This discrepancy is most likely due to different data sets that were used to compile the different locking maps.

Reduced interplate locking at an along-strike segment of the plate boundary is generally interpreted as a higher proportion of creep along the interface. In the present case, the upper plate seismicity that is situated above this locking low could indicate that a part of the apparent locking decrease comes from permanent deformation (instead of purely elastic buckling) of the upper plate. However, the magnitudes of the upper plate seismicity clusters we obtained are all quite small (nearly all earthquakes have M_L <3.5), so the released moment should be negligible compared to other forms of activity. This may imply that the process can not be responsible for the observed locking anomaly alone, or large earthquakes occur on significantly longer time scales than our 8 years of recording. The upper plate seismicity we record represents the brittle part of permanent upper plate deformation; offshore, where we see no upper plate seismicity, this deformation may occur plastically, or deformation could be purely elastic.

If an along-strike barrier, which is also apparent in the afterslip pattern of the Iquique earthquake (Hoffmann et al., 2018), is indeed present at ~21°S, an interesting question is whether this segmentation is permanent. A permanent segment boundary would imply that the area exhibits different rheological and/or frictional properties of the plate interface than elsewhere along strike, as has been proposed for the Mejillones Peninsula further south (Victor et al., 2011). Alternatively, the different observed seismological and geodetic signatures between the three parts of the plate interface (Iquique, Tocopilla and the area in-between; see Figure 12) may also be temporal, reflecting the different positions of the segments in the seismic cycle. The entire area encompassing the three parts we discuss here was last broken in 1877 (Comte & Pardo, 1991; Lomnitz, 2004). The 2007 Tocopilla earthquake that occurred in the early part of our observation period (see Figure S7) only broke the lower part of the plate interface (e.g., Peyrat et al., 2010; Schurr et al., 2012), which implies that the updip part of the interface should be in a very late stage of the seismic cycle. The same was true for the northern part of the study area throughout most of our observation period, until a mostly offshore asperity in this area finally broke on 1 April 2014, in the Iquique earthquake (see profiles A-A' to C-C' in Figure 6; Hayes et al., 2014; Ruiz et al., 2014; Schurr et al., 2014). Thus, at least the updip portion of the plate interface,

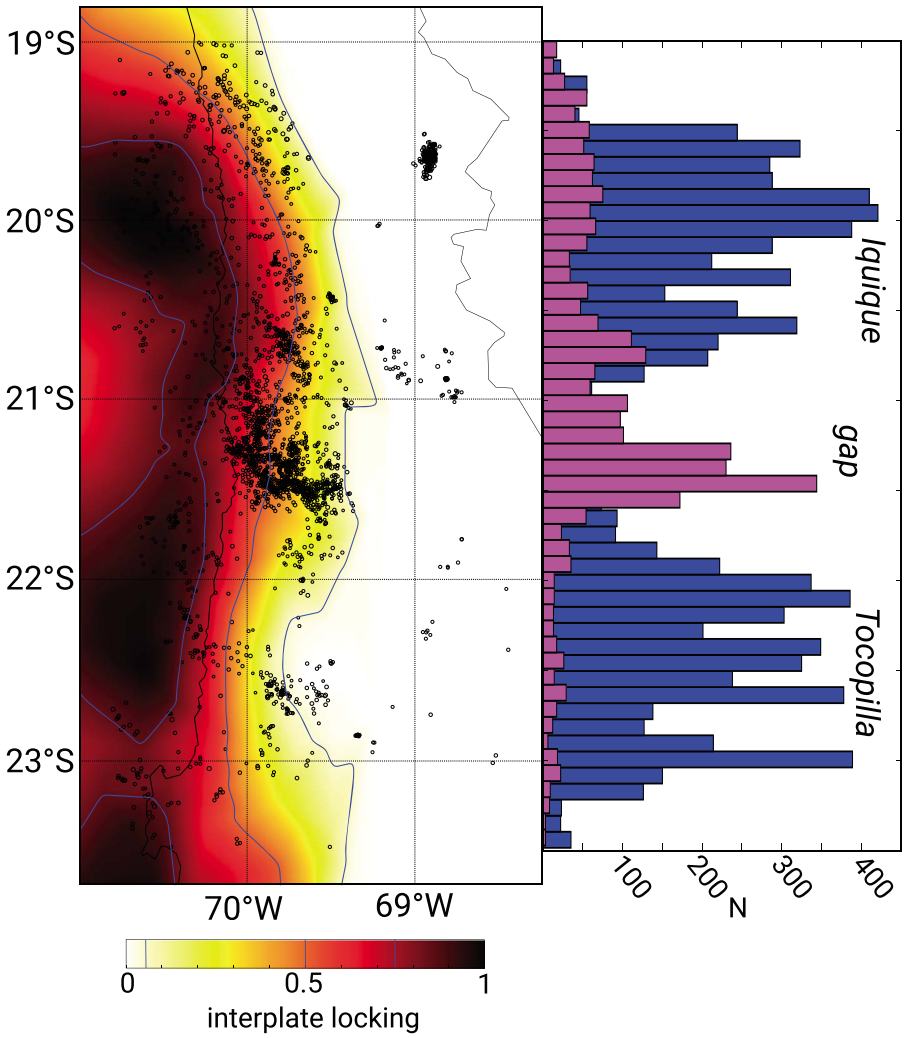

Figure 12. Map view of upper plate earthquakes, with events falling into the blasting time window removed (equivalent to Figure 7b), overlain with a map of interplate locking (Li et al., 2015; Moreno et al., 2016). The concentration of upper plate seismicity between 20.5 and 21.5°S appears to coincide with a patch of low interplate locking further offshore. In the right subplot, a histogram of event numbers with latitude is shown for plate interface events (blue) and upper plate events (magenta). We here removed upper plate earthquakes at depths shallower than 15 km in order to not capture the shallow seismicity cluster in the northeast. It can be seen that the upper plate earthquakes occur in a relative gap of interface seismicity between the aftershock series of the Tocopilla earthquake to the south and the Iquique earthquake to the north.

where the along-strike difference in locking is observed, should have been in a very similar position in the seismic cycle (unbroken since 1877) for all three segments of the plate interface we are considering.

The observed along-strike difference in both interplate locking and upper plate seismicity could thus represent different frictional properties of the plate interface at this latitude. It is also worth noting that the latitudinal position of the northern and southern ends of the proposed barrier correlate with the latitudes of the two offsets in intermediate-depth seismicity further downdip (see section 6.3.2; Figure 9). This could indicate that the internal structure and composition of the downgoing plate experiences a change at these locations, which then evokes the difference in locking and upper plate seismicity (see also section 7.4). Bloch et al. (2014) tentatively interpreted upper plate seismicity around 21°S as representing fluid ascent into the upper plate. Such a process (see more details in section 7.4) could provide an explanation for both the reduced interplate locking and the occurrence of upper plate seismicity in this area.

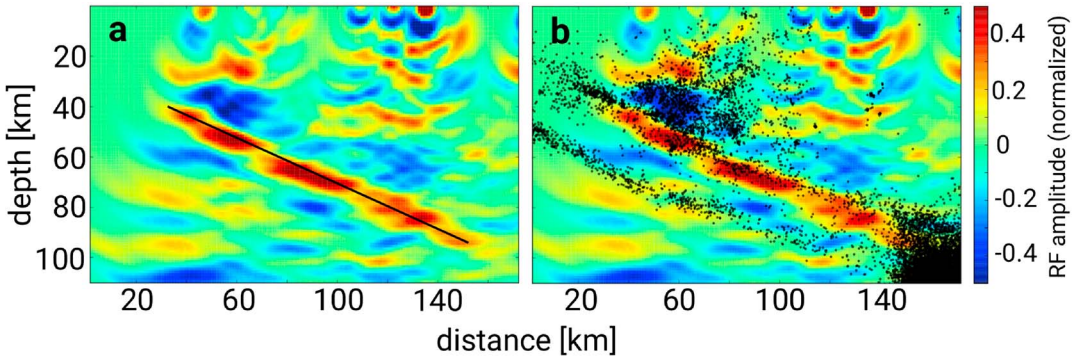

Figure 13. (a) Receiver function cross section along 21.2°S from Wölbern et al. (2009), remigrated using the velocity model of Husen et al. (1999). The Moho of the downgoing oceanic crust is imaged as a clear inclined anomaly (marked with black line) that disappears at a depth of ~90 km. (b) Earthquake hypocenters between 21 and 21.5°S, relocated in the same velocity model, plotted on top of the receiver functions. The start of the profile (0 km) is located at 70.5°W.

7.2. Are Upper Plane Intraslab Earthquakes Inside the Oceanic Crust or in the Mantle?

Downgoing oceanic crust in subduction zones has been imaged as a low-velocity layer atop the high-velocity slab with usually about 7–8 km thickness using receiver functions (e.g., Abers et al., 2006; Bostock, 2013; Rondenay et al., 2008) and guided wave observations (e.g., Abers, 2000; Martin et al., 2003). The downdip extent of this low-velocity layer varies between subduction zones and probably corresponds to the degree of basalt eclogitization in the downgoing crust (Peacock & Wang, 1999; Rondenay et al., 2008). To assert whether the upper plane of seismicity occurs within or slightly below the low-velocity layer is tricky due to depth uncertainties in the earthquake locations that can frequently be on the order of the thickness of the downgoing crust, as well as the caveat that hypocenters and receiver functions for the same subduction zone are often processed using different velocity models. Based on a careful analysis of seismicity distributions and receiver function images of the downgoing crust from a range of subduction zones, Abers et al. (2013) proposed that young and thus warm subducting slabs may exhibit upper and lower planes both located in the lithospheric mantle, whereas in colder slabs the upper plane is located within the downgoing crust.

At ~21.2°S, both an active (ANCORP; ANCORP Working Group, 1999; Oncken et al., 2003; Storch et al., 2016; Yoon et al., 2009) and a passive (ReFuCa; Wölbern et al., 2009) seismic profile have been acquired and analyzed. In Figure 13, we show an overlay of a seismicity cross section with the ReFuCa receiver function profile. To ensure that depths of converters and earthquakes are comparable, we used the same 1-D velocity model (from Husen et al., 1999) for both the migration of the receiver functions and the seismicity relocation (including double-difference processing). The receiver functions show a clear inclined positive (red) anomaly that disappears at a depth of ~90–100 km, which colocates with the inclined reflectivity high seen on the ANCORP active seismic profile (Oncken et al., 2003; Storch et al., 2016; Yoon et al., 2009) and is interpreted as the Moho of the downgoing oceanic crust. Earthquake hypocenters along the plate interface (blue in earlier figures) locate above the positive and below the overlying negative anomaly. The upper intraslab seismicity plane is colocated with the positive converter, indicating that these earthquakes occur close to the oceanic Moho (Figure 13b). It is interesting to note that the fine structure of the imaged Moho coverter, for example, the apparent offset at ~110-km distance, is mirrored by the hypocenters (Figure 13b). The colocation of the intraslab upper seismicity plane and the Moho converter disappears downdip, toward where the large band of intraslab seismicity commences, where upper plane earthquake hypocenters appear to gradually migrate above the imaged converter.

The oceanic crust currently entering the north Chile subduction zone is ~7 km thick (Patzwahl et al., 1999; Ranero & Sallarès, 2004), which corresponds to the distance between the upper two peaks in the hypocentral depth histogram relative to the slab surface (Figure 5). From these values alone, it is hard to determine on which side of the oceanic Moho the upper seismicity plane is located. If earthquakes are caused or triggered by prograde metamorphic dehydration reactions, a crustal upper seismicity plane would indicate lawsonite breakdown (Hacker, Peacock, et al., 2003), whereas a location in the uppermost oceanic mantle could be explained with brucite breakdown in serpentinized peridotite (e.g., Hyndman & Peacock, 2003). However, the observed gradual upward migration of earthquakes relative to the location of the oceanic Moho toward deeper depths favors location of seismicity in the oceanic crust. Close to where the upper plane merges

with the vigorous intermediate-depth event cluster, earthquakes are clearly above the oceanic Moho converter, hence in the crust. Were upper plane earthquakes further updip in the uppermost mantle, this would require two different processes causing upper plane events along dip, which could not easily reproduce the gradual upward migration we image. In the framework of Abers et al. (2013), northern Chile would thus qualify as a "colder" subduction zone, featuring an upper seismicity plane located within the downgoing crust. Why not the entire oceanic crust but only its deepest part seems to be seismogenic along most of the along-dip distance remains an open question.

Furthermore, it is noteworthy that both planes of intraslab seismicity are imaged as comparatively thin and sharp features, with widths of <5 km that are not much in excess of what we obtain for the subduction interface seismicity. In a more local study using a denser temporary network of seismic stations in the south of our study area, Fuenzalida et al. (2013) obtained a width of ~2 km for the plate interface or subduction channel (Cloos & Shreve, 1988) based on hypocenters from Tocopilla aftershocks, a value that falls into the range of widths obtained from fossil subduction channels identified in the rock record (e.g., Bachmann et al., 2009). For the two planes of intraslab earthquakes, however, we do not expect a discrete shear zone to host the seismicity, but the responsible processes should act on a rock volume. Thus, a maximum width of 5 km (since random location errors should always widen, never sharpen a feature, any widths obtained from hypocenters should be maximum estimates) is surprising and hints at reactions that are very tightly confined to the respective isotherm or property contrast, not allowing for prolonged metastability.

7.3. Slab Kink and the Joining of Seismicity Planes at Depths of 80–120 km

The lower end of the low-velocity layer imaged in Figure 13 coincides with where pervasive seismicity starts to occur in the intermediate-depth cluster (cyan color in Figures 6 and 11). It should be noted that the lower seismicity plane (red earthquakes), which has no clear expression in the receiver function image, is continuous into the lower edge of this intermediate-depth cluster (e.g., Figure 6, section D-D′). The lower planes of double seismic zones are commonly related to antigorite breakdown inside serpentinized mantle (e.g., Peacock, 2001). Figure 11 shows that the lower seismicity plane is oriented parallel to an isotherm, as would be expected for such a reaction. The retrieved temperature value of 600–650°C corresponds to the temperature range in which antigorite breakdown has been shown to occur (e.g., Plümper et al., 2016; Rüpke et al., 2004). At the transition to the intermediate-depth cluster, this correlation with an isotherm breaks down, and the entire mantle lithosphere above the lower plane isotherm, as well as most likely the overlying crust, is seismically active (Figures 11 and 13). Besides confirming the assertion by ANCORP Working Group (1999) that most of this slab seismicity is located in the mantle, this image resembles the plots of deserpentinization loci in Rüpke et al. (2004).

Since seismicity in the cluster sets in abruptly over its entire thickness, and hence does not follow the tapering of the isotherms, the process causing the earthquakes could be invoked by the slab entering the pressure regime necessary for the dehydration reaction of antigorite to occur at lower temperature. It is interesting to note that other subduction zones do not show a comparable feature: in the northern Honshu subduction zone, where high-resolution seismicity images are available (Hasegawa et al., 1978; Igarashi et al., 2001; Yamasaki & Seno, 2003), both seismicity planes remain separated. This may imply that the process causing this sudden onset of pervasive seismicity is controlled by temperature, as the Nazca slab is significantly younger and warmer. It is interesting to note that Kita et al. (2006) observed an increase of upper plane event numbers all along the northern Japan subduction zone at a depth of 70 to 100 km, which is comparable to the upper depth limit of the event cluster we found. However, seismicity there did not become pervasive between the planes, although a population of interplane events occurring further updip have been identified in the Japan subduction zone as well (Kita et al., 2010).

The observed increase in the Nazca slab's dip angle at a depth of ~100 km (see, e.g., Figure 10) is located close to the downdip termination of the pervasive slab seismicity. This likely implies that its origin is the density increase resulting from the dehydration of the serpentinized mantle rocks. Such slab kinks have been observed or postulated for a number of slabs (e.g., Klemd et al., 2011), but they are certainly not a feature common to all subduction zones. The Pacific slab under Northern Japan, for instance, shows a constant dip angle all the way to the mantle transition zone (e.g., Igarashi et al., 2001). Whether dip changes in slabs always correlate with an increase in intermediate-depth seismicity remains to be investigated. These possibly phase transformation-induced slab steepening processes may play a role in determining whether a subducting slab eventually penetrates into the lower mantle or becomes deflected and stagnant in the mantle transition zone.

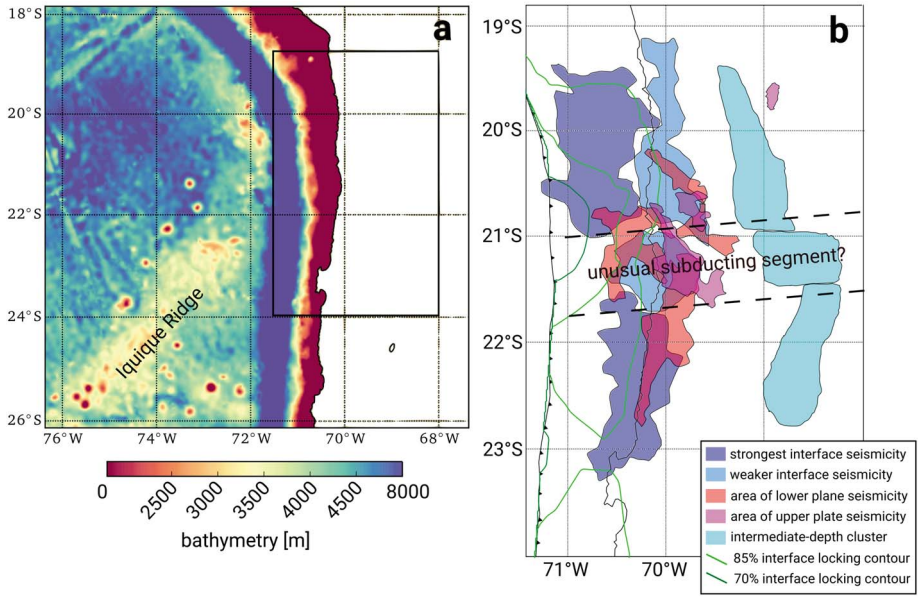

Figure 14. (a) Bathymetry map offshore of our study area. The Iquique Ridge shows up as a prominent, NE-SW striking feature. Black frame corresponds to the area depicted in subfigure b. (b) Synthesis of seismicity observations: Areas of high seismicity density in the different seismically active structures as well as interplate locking contours from the model shown in Figure 12 are displayed. For plate interface seismicity, the two different shadings of blue denote the most highly active areas during the two megathrust earthquake sequences (Tocopilla and Iquique; darker blue) and less active areas (lighter blue). It can be seen that the gap between the megathrust ruptures, the areas of increased upper plate and lower plane intraslab seismicity as well as the wider and more highly active segment in the deeper cluster all lie along a single downdip corridor that connects to the offshore interplate locking low observed with geodetic methods. This could indicate that an unusual (e.g., more highly hydrated) part of the downgoing plate is being subducted here.

Several slab segments that show a significant kink toward a steeper dip angle at intermediate depths, for example, Costa Rica (Protti et al., 1994), Java (Hall & Spakman, 2015), or northern Chile (this study), exhibit immediate penetration of the slab through the 670 (Fukao et al., 2001; Goes et al., 2017), whereas, for example, the slabs around Japan (Honshu, Izu-Bonin, and Kuriles), which feature constant dip angles, have been imaged as stagnating in the transition zone (Fukao et al., 2001; Goes et al., 2017; Zhao & Ohtani, 2009). Clearly, further research is necessary to check whether this speculative assertion holds under closer scrutiny.

7.4. Slab Hydration and the Subduction of Anomalous Lower Plate Features

The most peculiar observation that can be made from comparing Figures 3, 6, 8, and 12 is that the segment of the northern Chile subduction zone between 21 and 21.6°S differs from its surroundings in several ways: the lower plane of slab seismicity only reaches updip to shallow levels in this segment. Intermediate-depth seismicity is strongest in this latitude range and spans a larger range of depths than elsewhere along strike (see Figure 10). Moreover, pervasive upper plate seismicity, which is absent elsewhere, correlates with low offshore interplate locking here. These observations are summarized in Figure 14b.

We now propose a conceptual model that may explain these apparently coincident observations. Lower plane seismicity is thought to represent antigorite dehydration reactions occurring along an isotherm (~600–650°C) in the downgoing slab's mantle lithosphere (Hacker, Peacock, et al., 2003; Peacock, 2001). For these reactions, and thus lower plane seismicity, to occur, the slab mantle lithosphere has to be sufficiently hydrated and thus serpentinized at the outer rise or elsewhere (Faccenda, 2014; Ranero et al., 2003). The observed differences in lower plane seismicity rate between the central segment (profiles D-D' and E-E' in Figure 6) and the adjacent areas could thus be due to lower and/or less deeply penetrating slab hydration in the neighboring segments. If the maximum slab hydration depth is shallower than the isotherm that promotes the dehydration reaction, no lower plane seismicity is evoked. The shape and event rate of the intermediate-depth seismicity cluster is likewise dependent on slab hydration. Here the entire amount of serpentinized mantle between the isotherm traced by the lower plane earthquakes further updip and the oceanic crust experiences dehydration. Thus, the seismicity rate should correlate, to first order, with the amount of fluid that is present. The observed higher seismicity rate between 21 and 21.6°S thus suggests

a higher percentage of fluid present in the central segment of the northern Chile subduction zone (see along-strike event rate in Figure 3). This may also explain the difference in shape of the intermediate-depth cluster along strike: in the northern profiles (profiles A-A′, B-B′, Figures 6 and S6), the zone of intermediate-depth earthquakes appears to be thinner, and most earthquakes are found in the upper 5–10 km of this zone. This could imply that slab hydration at depths more than 10 km beneath the slab surface is weak and sporadic in this region. In profile D-D′, in contrast, the entire space between the depth level of the incoming lower seismicity plane and the oceanic crust is filled with seismicity, which hints at pervasive hydration of the slab (Figure S6).

The previously discussed two different loci of slab dehydration (lower plane and intermediate-depth cluster) affect two different parts of the overriding plate system: as shown in the topography swaths in Figure 6, the active intermediate-depth seismicity band is situated directly beneath the volcanic arc (e.g., Trumbull et al., 2006), indicating that slab dehydration drives melt generation in the mantle wedge, leading to arc volcanism (Tatsumi, 1986) and shallow hydrothermal systems like the Quebrada Blanca Bright Spot (ANCORP Working Group, 1999; Oncken et al., 2003). It is interesting to note that the Pica Volcanic gap (Wörner et al., 1992), an along-strike region in the northern Chile Cordillera that lacks any recent (i.e., <2 Ma) magmatism, is situated directly north of the slab seismicity offset we image at 21°S. Comte et al. (2016) have proposed a link between this volcanic gap and an along-strike change in subcrustal v_p/v_s ratio, which implies an along-strike variation in mantle wedge hydration state.

Dehydration reactions in the lower seismicity plane, in contrast, may influence the behavior of the plate interface and thus change the coupling between the plates. Moreno et al. (2014) have shown that interplate locking in Central Chile appears to anticorrelate with Poisson ratio near the plate interface, which is taken as an indicator for fluid pressure. If fluids are released in the lower plane and transported into the megathrust shear zone, this could reduce normal stress and thus the locking degree and possibly change the frictional behavior to conditionally stable or stable (Scholz & Campos, 2012). Alternatively, the presence and activity of the lower seismicity plane could simply be a proxy for the amount of water inside the entire slab segment, and thus, hydration around 21–21.6°S should also be elevated in the oceanic crust, which could likewise lead to an increase in interface lubrication (Figures 12 and 11).

A possible explanation for the proposed along-strike change in slab hydration is provided by the presence of the Iquique Ridge offshore the study area. This SW-NE trending broad bathymetric feature offshore northern Chile impinges onto the trench roughly between 21 and 23°S (e.g., Contreras-Reyes & Carrizo, 2011; Gutscher et al., 2000). It has been shown to consist, at least locally, of substantially thickened crust (locally up to 15 km thick according to Tassara et al., 2006) offshore and has been classified as an "aseismic ridge," that is, of hot spot-related origin, by Rosenbaum and Mo (2011). Aseismic ridges have been shown to be more strongly hydrated than other oceanic areas (Faccenda, 2014), and the subduction of bathymetric anomalies has been linked with decreased interplate coupling (Wang & Bilek, 2014). Moreover, correlations between the presence of subducting seafloor anomalies and changes in seismicity rate and/or style due to differences in hydration have been proposed elsewhere (e.g., Ranero et al., 2003; Shillington et al., 2015).

However, direct evidence that the Iquique Ridge is currently being subducted in northern Chile is lacking, although its bathymetric signature (see Figure 14a) abuts the trench. In the framework of the CINCA95 project, a series of active seismic profiles crossing the oceanic trench between ~19 and 26°S were acquired in the late 1990s. Just offshore Antofagasta, that is, south of our study area, a crustal thickness of 7 km (±0.5 km) was imaged at the trench (Ranero & Sallarès, 2004). For all of the profiles, Patzwahl et al. (1999) noted that assuming the worldwide average crustal thickness of 7 km (Bown & White, 1994) fits the observed arrival time patterns.

On the other hand, the Iquique Ridge is anything but a regular feature in bathymetry and crustal thickness (Tassara et al., 2006), so it is conceivable that a part of it that features relatively normal oceanic crust is currently at the trench, whereas more anomalous crust may have been subducted in the past. Such a scenario could explain most of the observations listed above. At an aseismic ridge, hydration of oceanic crust and mantle lithosphere should be stronger and likely also penetrate to deeper depths, than for normal oceanic lithosphere (Faccenda, 2014). Thus, the distribution of lower plane activity shown in Figure 8 would correspond to the distribution of deep mantle lithospheric hydration and would provide a rough "map" of subducted anomalous material. On the plate interface, this increased hydration, and/or the presence of subducted seafloor relief itself, could be responsible for the observed locking low (Figures 12 and 14). In a sediment-starved margin

like northern Chile (von Huene & Scholl, 1991), increased lubrication or subduction of rough seafloor (e.g., Wang & Bilek, 2014) is the principal mechanism of how an increased proportion of creep at the plate interface can be explained. How exactly this relates to the observation of increased upper plate seismicity above the partially creeping segment is currently unclear and requires further research (see also section 7.1). One possible hypothesis is that upper plate earthquakes represent fluid ascent into the upper plate (e.g., Bloch et al., 2014), which would directly link them to the deeper processes. Further downdip, the observation of a more highly active piece of slab at intermediate depths between ~21 and 21.6°S could further trace the subducted anomalous crust and lithosphere along its descent (Figure 14). Kirby, Engdahl, and Denlinger (1996) have proposed that subducting bathymeric features cause streaks of increased intermediate-depth seismicity elsewhere along the south American margin. The observed offset between slab earthquakes north and south of the anomalously active structure (Figures 9 and 10), however, remains enigmatic even in this scenario. Speculatively, one could invoke a difference in composition and/or thermal structure of the slab to explain the observations.

8. Conclusions

We analyzed 8 years of continuous seismic data (2007–2014) from the IPOC network in northern Chile and auxiliary stations and retrieved a seismicity catalog containing >100,000 double-difference relocated earthquake hypocenters. Intraslab seismicity makes up more than 60% of our data set and can be subdivided into a vigorous, 25 km wide band of intermediate-depth seismicity that is observed at ~80- to 140-km depth, sporadic seismicity in clusters downdip of it, and slab seismicity further updip that defines three narrow planes.

Activity on the uppermost of these planes, which is interpreted as the plate interface, is mainly confined to the aftershock series of large megathrust events (M7.7 Tocopilla 2007 and M8.1 Iquique 2014). Earthquakes at the plate interface sharply terminate downdip at about 50- to 55-km depth. The upper plane, located about 6–7 km below the plate interface, shows spatially homogeneous seismicity in the entire study area. Based on a receiver function image, we interpret these earthquakes as representing dehydration reactions, possibly lawsonite breakdown, in the lowermost oceanic crust. At 25–27 km below the plate interface, the lower plane of intraslab seismicity is clearly located inside the oceanic mantle lithosphere of the downgoing plate and most likely represents antigorite dehydration reactions of serpetinites. Unlike the upper plane, the lower serpentinites plane is not observed everywhere in the study area, and its seismicity forms clusters that may reflect along-strike changes in hydration depth of the downgoing plate.

At a depth of about 80 km, the gap between upper and lower plane seismicity is abruptly closed, and a highly active cluster of ~25 km thickness is present everywhere along the strike of our study area. This appears to indicate that all of the hydrated mantle lithospheric serpentinite that is present in the downgoing plate starts to dehydrate at this depth, regardless of the temperature field. We also observed seismicity in the upper plate, which is strongest in a region around 21°S. This region of upper plate earthquakes has a well-defined, E-W striking southern termination just south of the Rio Loa. Interestingly, this concentration of upper plate activity spatially correlates with an offshore low in interplate locking as well as the gap between the Tocopilla and Iquique earthquake rupture areas on the plate interface.

When combining our observations (Figure 14), we obtain a clear indication that the segment of the north Chile subduction zone between 21 and 21.6°S is different from the rest of the study area. Both lower plane and upper plate seismicity are strongest there, the strong band of intermediate-depth earthquake spans a wider range along dip and exhibits a higher seismicity rate, and seismicity on the interface is lower than elsewhere since this segment did not rupture in a recent megathrust earthquake. Taken together, these observations could be interpreted as the ongoing subduction of unusual oceanic material beneath this area, possibly a part of the Iquique Ridge. Such material should be more strongly hydrated than the oceanic lithospere elsewhere, which should spark more dehydration-related seismicity, while at the same time inhibiting major seismicity on the plate interface by more strongly lubricating the interface, which leads to a higher proportion of aseismic creep.

The seismicity catalog produced and analyzed in this study is available from the supporting information to this article and from Sippl et al. (2018).

Acknowledgments
This research was funded by Deutsche Forschungsgemeinschaft (SCHU 2460/3-1) and GFZ Potsdam. The analyzed seismic waveform data came from the IPOC network (GFZ & CNRS-INSU, 2006), GEOFON station LVC (GEOFON Data Center, 1993), the Chilean networks C and C1 (accessed via the IRIS data center: http://ds.iris.edu/SeismiQuery/), as well as the temporary deployments MINAS (Asch et al., 2011), WestFissure (Wigger et al., 2016) and IQ. We acknowledge discussions with Timm John, Onno Oncken and Wasja Bloch. We are grateful for constructive reviews by Diana Comte and Geoff Abers that helped us to improve the manuscript.

References

Abers, G. A. (2000). Hydrated subducted crust at 100–250 km depth. *Earth and Planetary Science Letters*, *176*(3–4), 323–330. https://doi.org/10.1016/S0012-821X(00)00007-8

Abers, G. A., Nakajima, J., Van Keken, P. E., Kita, S., & Hacker, B. R. (2013). Thermal-petrological controls on the location of earthquakes within subducting plates. *Earth and Planetary Science Letters*, *369–370*, 178–187. https://doi.org/10.1016/j.epsl.2013.03.022

Abers, G. A., Van Keken, P. E., Kneller, E. A., Ferris, A., & Stachnik, J. C. (2006). The thermal structure of subduction zones constrained by seismic imaging: Implications for slab dehydration and wedge flow. *Earth and Planetary Science Letters*, *241*(3–4), 387–397. https://doi.org/10.1016/j.epsl.2005.11.055

Aldersons, F. (2004). Toward a three-dimensional crustal structure of the Dead Sea region from local earthquake tomography (PhD Thesis), Tel-Aviv University.

Allmendinger, R. W., & González, G. (2010). Invited review paper: Neogene to Quaternary tectonics of the coastal Cordillera, northern Chile. *Tectonophysics*, *495*(1–2), 93–110. https://doi.org/10.1016/j.tecto.2009.04.019

ANCORP Working Group (1999). Seismic reflection image revealing offset of Andean subduction-zone earthquake locations into oceanic mantle. *Nature*, *397*, 341–344. https://doi.org/10.1038/16909

Angermann, D., Klotz, J., & Reigber, C. (1999). Space-geodetic estimation of the Nazca-South America Euler vector. *Earth and Planetary Science Letters*, *171*(3), 329–334. https://doi.org/10.1016/S0012-821X(99) 00173-9

Asch, G., Tilmann, F., Schurr, B., & Ryberg, T. (2011). Seismic network 5E: MINAS project (2011/2013) (*Tech. rep.*) Potsdam: Deutsches GeoForschungsZentrum GFZ. https://doi.org/10.14470/ab466166

Bachmann, R., Oncken, O., Glodny, J., Seifert, W., Georgieva, V., & Sudo, M. (2009). Exposed plate interface in the European Alps reveals fabric styles and gradients related to an ancient seismogenic coupling zone. *Journal of Geophysical Research*, *114*, B05402. https://doi.org/10.1029/2008JB005927

Benioff, H. (1949). Seismic evidence for the fault origin of oceanic deeps. *Bulletin of the Geological Society of America*, *60*(12), 1837–1856. https://doi.org/10.1130/0016-7606(1949)60[1837:GROTIO]2.0.CO;2

Bloch, W., Kummerow, J., Salazar, P., Wigger, P., & Shapiro, S. A. (2014). High-resolution image of the North Chilean subduction zone: Seismicity, reflectivity and fluids. *Geophysical Journal International*, *197*(3), 1744–1749. https://doi.org/10.1093/gji/ggu084

Bostock, M. G. (2013). The Moho in subduction zones. *Tectonophysics*, *609*, 547–557. https://doi.org/10.1016/j. tecto.2012.07.007

Bown, J. W., & White, R. S. (1994). Variation with spreading rate of oceanic crustal thickness and geochemistry. *Earth and Planetary Science Letters*, *121*(3–4), 435–449. https://doi.org/10.1016/0012-821X(94)90082-5

Brudzinski, M. R., Thurber, C. H., Hacker, B. R., & Engdahl, E. R. (2007). Global prevalence of double Benioff zones. *Science*, *316*(5830), 1472–1474. https://doi.org/10.1126/science.1139204

Cahill, T., & Isacks, B. (1992). Seismicity and shape of the subducted Nazca Plate. *Journal of Geophysical Research*, *97*(B12), 17,503–17,529. https://doi.org/10.1029/92JB00493

Cesca, S., Grigoli, F., Heimann, S., Dahm, T., Kriegerowski, M., Sobiesiak, M., et al. (2016). The *M*w 8.1 2014 Iquique, Chile, seismic sequence: A tale of foreshocks and aftershocks. *Geophysical Journal International*, *204*(3), 1766–1780. https://doi.org/10.1093/gji/ggv544

Cloos, M., & Shreve, R. (1988). Subduction-channel model of prism accretion, melange formation, sediment subduction, and subduction erosion at convergent plate margins: 1. Background and description. *Pure and Applied Geophysics*, *128*(3/4), 455–500.

Comte, D., & Pardo, M. (1991). Reappraisal of great historical earthquakes in the northern Chile and southern Peru seismic gaps. *Natural Hazards*, *4*(1), 23–44. https://doi.org/10.1007/BF00126557

Comte, D., Carrizo, D., Roecker, S. W., Ortega-Culaciati, F., & Peyrat, S. (2016). Three-dimensional elastic wave speeds in the northern Chile subduction zone: Variations in hydration in the supraslab mantle. *Geophysical Journal International*, *207*(2), 1080–1105. https://doi.org/10.1093/gji/ggw318

Comte, D., Dorbath, L., Pardo, M., Monfret, T., Haessler, H., Rivera, L., et al. (1999). A double layered seismic zone in Arica, northern Chile. *Geophysical Research Letters*, *26*(13), 1965–1968. https://doi.org/10.1029/1999GL900447

Contreras-Reyes, E., & Carrizo, D. (2011). Control of high oceanic features and subduction channel on earthquake ruptures along the Chile-Peru subduction zone. *Physics of the Earth and Planetary Interiors*, *186*(1–2), 49–58. https://doi.org/10.1016/j.pepi.2011.03.002

Di Stefano, R., Aldersons, F., Kissling, E., Baccheschi, P., Chiarabba, C., & Giardini, D. (2006). Automatic seismic phase picking and consistent observation error assessment: Application to the Italian seismicity. *Geophysical Journal International*, *165*(1), 121–134. https://doi.org/10.1111/j.1365-246X.2005.02799.x

Diehl, T., Deichmann, N., Kissling, E., & Husen, S. (2009). Automatic S-wave picker for local earthquake tomography. *Bulletin of the Seismological Society of America*, *99*(3), 1906–1920. https://doi.org/10.1785/0120080019

Dorbath, C., Gerbault, M., Carlier, G., & Guiraud, M. (2008). Double seismic zone of the Nazca plate in northern Chile: High-resolution velocity structure, petrological implications, and thermomechanical modeling. *Geochemistry, Geophysics, Geosystems*, *9*, Q07006. https://doi.org/10.1029/2008GC002020

Eberhart-Phillips, D. (1986). Three-dimensional velocity structure in northern California Coast Ranges from inversion of local earthquake arrival times. *Bulletin of the Seismological Society of America*, *76*(4), 1025–1052.

Engdahl, E. R., Van der Hilst, R., & Buland, R. (1998). Global teleseismic earthquake relocation with improved travel times and procedures for depth determination. *Bulletin of the Seismological Society of America*, *88*(3), 722–743. https://doi.org/10.1130/0-8137-2349-3.461

Evans, J. R., Eberhart-Phillips, D., & Thurber, C. H. (1994). User's manual for SIMULPS12 for imaging vp and vp/vs: A derivative of the "Thurber" tomographic inversion SIMUL3 for local earthquakes and explosions (*Tech. rep. Open File Report 94-431*). US Geological Survey: US Department of the Interior.

Faccenda, M. (2014). Water in the slab: A trilogy. *Tectonophysics*, *614*, 1–30. https://doi.org/10.1016/j.tecto. 2013.12.020

Fuenzalida, A., Schurr, B., Lancieri, M., Sobiesiak, M., & Madariaga, R. (2013). High-resolution relocation and mechanism of aftershocks of the 2007 Tocopilla (Chile) earthquake. *Geophysical Journal International*, *194*(2), 1216–1228. https://doi.org/10.1093/gji/ggt163

Fukao, Y., Widiyantoro, S., & Obayashi, M. (2001). Stagnant slabs in the upper and lower mantle transition region. *Reviews of Geophysics*, *39*(1999), 291–323. https://doi.org/10.1029/1999rg000068

Garth, T., & Rietbrock, A. (2017). Constraining the hydration of the subducting Nazca plate beneath Northern Chile using subduction zone guided waves. *Earth and Planetary Science Letters*, *474*, 237–247. https://doi.org/10.1016/j.epsl.2017.06.041

GEOFON Data Center (1993). GEOFON Seismic Network (Tech. Rep.) Potsdam: Deutsches GeoForschungsZentrum GFZ. https://doi.org/10.14470/TR560404

GFZ, & CNRS-INSU (2006). IPOC seismic network. Integrated Plate boundary Observatory Chile-IPOC (Tech. rep.): German Research Centre for Geosciences and Institut des Sciences de l'Univers-Centre National de la Recherche. https://doi.org/10.14470/PK615318

Goes, S., Agrusta, R., van Hunen, J., & Garel, F. (2017). Subduction-transition zone interaction: A review. *Geosphere*, *13*(3), 644–664. https://doi.org/10.1130/GES01476.1

González, G., Dunai, T., Carrizo, D., & Allmendinger, R. W. (2006). Young displacements on the Atacama Fault System, northern Chile from field observations and cosmogenic ^{21}Ne concentrations. *Tectonics*, *25*, TC3006. https://doi.org/10.1029/2005TC001846

Graeber, F., & Asch, G. (1999). Three-dimensional models of *P* wave velocity and *P*-to-*S* velocity ratio in the southern central Andes by simultaneous inversion of local earthquake data. *Journal of Geophysical Research*, *104*(B9), 20,237–20,256. https://doi.org/10.1029/1999JB900037

Gutscher, M. A., Olivet, J. L., Aslanian, D., Eissen, J. P., & Maury, R. (1999). The "lost Inca Plateau": Cause of flat subduction beneath Peru? *Earth and Planetary Science Letters*, *171*(3), 335–341. https://doi.org/10.1016/S0012-821X(99)00153-3

Gutscher, M. A., Spakman, W., Bijwaard, H., & Engdahl, E. R. (2000). Geodynamics of flat subduction: Seismicity and tomographic constraints from the Andean margin. *Tectonics*, *19*(5), 814–833. https://doi.org/10.1029/1999TC001152

Hacker, B. R., Abers, G. A., & Peacock, S. M. (2003). Subduction factory 1. Theoretical mineralogy, densities, seismic wave speeds, and H_2O contents. *Journal of Geophysical Research*, *108*, 2029. https://doi.org/10.1029/2001JB001127

Hacker, B. R., Peacock, S. M., Abers, G. A., & Holloway, S. D. (2003). Subduction factory 2. Are intermediate-depth earthquakes in subducting slabs linked to metamorphic dehydration reactions? *Journal of Geophysical Research*, *108*, 2030. https://doi.org/10.1029/2001JB001129

Hall, R., & Spakman, W. (2015). Mantle structure and tectonic history of SE Asia. *Tectonophysics*, *658*, 14–45. https://doi.org/10.1016/j.tecto.2015.07.003

Hasegawa, A., Horiuchi, S., & Umino, N. (1978). Seismic structure of the northeastern Japan convergent margin: A synthesis. *Journal of Geophysical Research*, *99*(B11), 22,295–22,311. https://doi.org/10.1029/93JB02797

Hasegawa, A., Umino, N., & Takagi, A. (1978). Double-planed deep seismic zone and upper mantle structure in the northeastern Japan arc. *Geophysical Journal of the Royal Astronomical Society*, *54*, 281–296.

Hayes, G., Herman, M. W., Barnhart, W. D., Furlong, K. P., Riquelme, S., Benz, H., et al. (2014). Continuing megathrust earthquake potential in Chile after the 2014 Iquique earthquake. *Nature*, *512*, 295–298. https://doi.org/10.1038/nature13677

Hayes, G., Wald, D. J., & Johnson, R. L. (2012). Slab1.0: A three-dimensional model of global subduction zone geometries. *Journal of Geophysical Research*, *117*, B01302. https://doi.org/10.1029/2011JB008524

Hoffmann, F., Metzger, S., Moreno, M., Deng, Z., Sippl, C., Ortega-Culaciati, F., & Oncken, O. (2018). Characterizing afterslip and ground displacement rate increase following the 2014 Iquique-Pisagua Mw 8.1 earthquake, Northern Chile. *Journal of Geophysical Research: Solid Earth*, *123*. https://doi.org/10.1002/2017JB014970

Holtkamp, S., & Brudzinski, M. R. (2014). Megathrust earthquake swarms indicate frictional changes which delimit large earthquake ruptures. *Earth and Planetary Science Letters*, *390*, 234–243. https://doi.org/10.1016/j.epsl.2013.10.033

Husen, S., Kissling, E., Flueh, E. R., & Asch, G. (1999). Accurate hypocenter determination in the shallow part of the Nazca subduction one in Northern Chile using a combined on-/offshore network. *Geophysical Journal International*, *138*, 687–701.

Hutton, L. K., & Boore, D. M. (1987). The Ml Scale in Southern California. *Bulletin Of The Seismological Society Of America*, *77*(6), 2074–2094.

Hyndman, R. D., & Peacock, S. M. (2003). Serpentinization of the forearc mantle. *Earth and Planetary Science Letters*, *212*(3–4), 417–432. https://doi.org/10.1016/S0012-821X(03)00263-2

Igarashi, T., Matsuzawa, T., Umino, N., & Hasegawa, A. (2001). Spatial distribution of focal mechanisms for interplate and intraplate earthquakes associated with the subducting Pacific plate beneath the northeastern Japan arc: A triple-planed deep seismic zone. *Journal of Geophysical Research*, *106*(B2), 2177–2191. https://doi.org/10.1029/2000JB900386

Jarrard, R. D. (1986). Relations among subduction parameters. *Reviews of Geophysics*, *24*(2), 217–284. https://doi.org/10.1029/RG024i002p00217

John, T., Medvedev, S., Rüpke, L. H., Andersen, T., Podladchikov, Y. Y., & Austrheim, H. (2009). Generation of intermediate-depth earthquakes by self-localizing thermal runaway. *Nature Geoscience*, *2*(2), 137–140. https://doi.org/10.1038/ngeo419

Jung, H., Green, H. W., & Dobrzhinetskaya, L. F. (2004). Intermediate-depth earthquake faulting by dehydration embrittlement with negative volume change. *Nature*, *428*(6982), 545–549. https://doi.org/10.1038/nature02412

Kelemen, P., & Hirth, G. (2007). A periodic shear-heating mechanism for intermediate-depth earthquakes in the mantle. *Nature*, *446*(7137), 787–790. https://doi.org/10.1038/nature05717

Kerrick, D. M., & Connolly, J. A. D. (2001). Metamorphic devolatilization of subducted oceanic metabasalts: Implications for seismicity, arc magmatism and volatile recycling. *Earth and Planetary Science Letters*, *189*(1–2), 19–29. https://doi.org/10.1016/S0012-821X(01)00347-8

Kirby, S., Durham, W. B., & Stern, L. A. (1991). Mantle phase changes and deep-earthquake faulting in subducting lithosphere. *Science*, *252*(5003), 216–225. https://doi.org/10.1126/science.252.5003.216

Kirby, S., Stein, S., Okal, E., & Rubie, D. C. (1996). Metastable mantle phase transformations and deep earthquakes in subducting oceanic lithosphere. *Reviews of Geophysics*, *34*(2), 261–306. https://doi.org/10.1029/96RG01050

Kirby, S., Engdahl, E. R., & Denlinger, R. (1996). Intermediate-depth intraslab earthquakes and arc volcanism as physical expressions of crustal and uppermost mantle metamorphism in subducting slabs. In G. Bebout, et al. (Eds.), *Subduction top to bottom, Geophysical Monograph Series* (Vol. 96, pp.195–214). Washington DC: American Geophysical Union.

Kissling, E., Ellsworth, W. L., Eberhart-Phillips, D., & Kradolfer, U. (1994). *Journal of Geophysical Research*, *99*(B10), 19,635–19,646.

Kita, S., Okada, T., Nakajima, J., Matsuzawa, T., & Hasegawa, A. (2006). Existence of a seismic belt in the upper plane of the double seismic zone extending in the along-arc direction at depths of 70–100 km beneath NE Japan. *Geophysical Research Letters*, *24*, L24310. https://doi.org/10.1029/2006GL028239

Kita, S., Okada, T., Hasegawa, A., Nakajima, J., & Matsuzawa, T. (2010). Existence of interplane earthquakes and neutral stress boundary between the upper and lower planes of the double seismic zone beneath Tohoku and Hokkaido, northeastern Japan. *Tectonophysics*, *496*(1–4), 68–82. https://doi.org/10.1016/j.tecto.2010.10.010

Klemd, R., John, T., Scherer, E. E., Rondenay, S., & Gao, J. (2011). Changes in dip of subducted slabs at depth: Petrological and geochronological evidence from HP-UHP rocks (Tianshan, NW-China). *Earth and Planetary Science Letters*, *310*(1–2), 9–20. https://doi.org/10.1016/j.epsl.2011.07.022

Lange, D., Tilmann, F., Barrientos, S., Contreras-Reyes, E., Methe, P., Moreno, M., et al. (2012). Aftershock seismicity of the 27 February 2010 Mw 8.8 Maule earthquake rupture zone. *Earth and Planetary Science Letters*, *317-318*(February 2010), 413–425. https://doi.org/10.1016/j.epsl.2011.11.034

Lay, T., Kanamori, H., Ammon, C. J., Koper, K. D., Hutko, A. R., Ye, L., et al. (2012). Depth-varying rupture properties of subduction zone megathrust faults. *Journal of Geophysical Research*, *117*, B04311. https://doi.org/10.1029/2011JB009133

Li, S., Moreno, M., Bedford, J., Rosenau, M., & Oncken, O. (2015). Revisiting viscoelastic effects on interseismic deformation and locking degree: A case study of the Peru-North Chile subduction zone. *Journal of Geophysical Research: Solid Earth*, *120*, 4522–4538. https://doi.org/10.1002/2015JB011903

Lomax, A., Virieux, J., Volant, P., & Berge-thierry, C. (2000). Chapter 5 Probabilistic earthquake location in 3D and layered models. In A. Lomax, et al. (Eds.), *Advances in Seismic Event Location* (pp. 101–134). Amsterdam: Kluwer Academic Publishers.

Lomnitz, C. (2004). Major Earthquakes of Chile: A Historical Survey, 1535-1960. *Seismological Research Letters*, *75*(3), 368–378. https://doi.org/10.1785/gssrl.75.3.368

Martin, S., Rietbrock, A., Haberland, C., & Asch, G. (2003). Guided waves propagating in subducted oceanic crust. *Journal of Geophysical Research*, *108*(B11), 2536. https://doi.org/10.1029/2003JB002450

Melnick, D., Moreno, M., Motagh, M., Cisternas, M., & Wesson, R. L. (2012). Splay fault slip during the Mw 8.8 2010 Maule Chile earthquake. *Geology*, *40*(3), 251–254. https://doi.org/10.1130/G32712.1

Métois, M., Socquet, A., Vigny, C., Carrizo, D., Peyrat, S., Delorme, A., et al. (2013). Revisiting the North Chile seismic gap segmentation using GPS-derived interseismic coupling. *Geophysical Journal International*, *194*(3), 1283–1294. https://doi.org/10.1093/gji/ggt183

Mittelstädt, J., Victor, P., & Radeisen, N. (2018). The link between megathrust segmentation and upper plate faulting along the N-Chilean subduction system. *Geophysical Research Abstracts*, *20*, EGU2018–15337–1.

Moreno, M., Haberland, C., Oncken, O., Rietbrock, A., Angiboust, S., & Heidbach, O. (2014). Locking of the Chile subduction zone controlled by fluid pressure before the 2010 earthquake. *Nature Geoscience*, *7*(4), 292–296. https://doi.org/10.1038/ngeo2102

Moreno, M., Metzger, S., Bedford, J., Hoffmann, F., Li, S., Deng, Z., et al. (2016). Satellitengeodäsie und Erdbeben deformation in der nordchilenischen seismischen Lücke. *System Erde*, *6*(2), 36–41. https://doi.org/10.2312/GFZ.syserde.06.02.6

Nocquet, J. M., Villegas-Lanza, J. C., Chlieh, M., Mothes, P. A., Rolandone, F., Jarrin, P., et al. (2014). Motion of continental slivers and creeping subduction in the northern Andes. *Nature Geoscience*, *7*(4), 287–291. https://doi.org/10.1038/ngeo2099

Norabuena, E., Leffler-Griffin, L., Mao, A., Dixon, T., Stein, S., Sacks, S., et al. (1998). Space geodetic observations of Nazca-South America convergence across the central andes. *Science*, *279*, 358–362. https://doi.org/10.1126/science.279.5349.358

Okazaki, K., & Hirth, G. (2016). Dehydration of lawsonite could directly trigger earthquakes in subducting oceanic crust. *Nature*, *530*, 81–84. https://doi.org/10.1038/nature16501

Oleskevich, D. A., Hyndman, R. D., & Wang, K. (1999). The updip and downdip limits to great subduction earthquakes: Thermal and structural models of Cascadia, south Alaska, SW Japan, and Chile. *Journal of Geophysical Research*, *104*(B7), 14,965–14,991. https://doi.org/10.1029/1999JB900060

Oncken, O., Sobolev, S. V., Stiller, M., Asch, G., Haberland, C., Mechie, J., et al. (2003). Seismic imaging of a convergent continental margin and plateau in the central Andes (Andean Continental Research Project 1996 (ANCORP'96). *Journal of Geophysical Research*, *108*(7), 2328. https://doi.org/10.1029/2002JB001771

Park, J.-O., Tsuru, T., Kodaira, S., Cummins, P. R., & Kaneda, Y. (2002). Splay fault branching along the Nankai subduction zone. *Science*, *297*, 1157–1160. https://doi.org/10.1126/science.1074111

Patzwahl, R., Mechie, J., Schulze, A., & Giese, P. (1999). Two-dimensional velocity models of the Nazca Plate subduction zone between 19.5S and 25S from wide-angle seismic measurements during the CINCA95 project. *Journal of Geophysical Research*, *104*(B4), 7293–7317. https://doi.org/10.1029/1999JB900008

Pavlis, G. L. (1986). Appraising earthquake hypocenter location errors: A complete, practical approach for single-event locations. *Bulletin of the Seismological Society of America*, *76*(6), 1699–1717.

Peacock, S. M. (2001). Are the lower planes of double seismic zones caused by serpentine dehydration in subducting oceanic mantle? *Geology*, *29*(4), 299–302. https://doi.org/10.1130/0091-7613(1980)?8<11:APCAKM>?2.0.CO

Peacock, S. M., & Wang, K. (1999). Seismic consequences of warm versus cool subduction metamorphism: Examples from southwest and northeast Japan. *Science*, *286*, 937–939. https://doi.org/10.1126/science.286.5441.937

Perfettini, H., Avouac, J. P., & Ruegg, J. C. (2005). Geodetic displacements and aftershocks following the 2001 $M_w = 8.4$ Peru earthquake: Implications for the mechanics of the earthquake cycle along subduction zones. *Journal of Geophysical Research*, *110*, B09404. https://doi.org/10.1029/2004JB003522

Peyrat, S., Madariaga, R., Buforn, E., Campos, J., Asch, G., & Vilotte, J. P. (2010). Kinematic rupture process of the 2007 Tocopilla earthquake and its main aftershocks from teleseismic and strong-motion data. *Geophysical Journal International*, *182*(3), 1411–1430. https://doi.org/10.1111/j.1365-246$\times$. 2010.04685.x

Plümper, O., John, T., Podladchikov, Y. Y., Vrijmoed, J. C., & Scambelluri, M. (2016). Fluid escape from subduction zones controlled by channel-forming reactive porosity. *Nature Geoscience*, *10*(2), 150–156. https://doi.org/10.1038/ngeo2865

Protti, M., Gündel, F., & McNally, K. (1994). The geometry of the Wadati-Benioff zone under southern Central America and its tectonic significance: Results from a high-resolution local seismographic network. *Physics of the Earth and Planetary Interiors*, *84*, 271–287. https://doi.org/10.1130/SPE295

Ramos, V. A., Cristallini, E. O., & Perez, D. J. (2002). The Pampean flat-slab of the Central Andes. *Journal of South American Earth Sciences*, *15*(1), 59–78. https://doi.org/10.1016/S0895-9811(02)00006-8

Ranero, C. R., & Sallarès, V. (2004). Geophysical evidence for hydration of the crust and mantle of the Nazca plate during bending at the north Chile trench. *Geology*, *32*(7), 549–552. https://doi.org/10.1130/G20379.1

Ranero, C. R., Phipps Morgan, J., McIntosh, K., & Reichert, C. (2003). Bending-related faulting and mantle serpentinization at the Middle America trench. *Nature*, *425*(6956), 367–373. https://doi.org/10.1038/nature01961

Reyners, M., Eberhart-Phillips, D., & Bannister, S. (2011). Tracking repeated subduction of the Hikurangi Plateau beneath New Zealand. *Earth and Planetary Science Letters*, *311*(1–2), 165–171. https://doi.org/10.1016/j.epsl.2011.09.011

Rietbrock, A., & Waldhauser, F. (2004). A narrowly spaced double-seismic zone in the subducting Nazca plate. *Geophysical Research Letters*, *31*, L10608. https://doi.org/10.1029/2004GL019610

Rietbrock, A., Haberland, C., & Nippress, S. (2008). A tear in the subducting Nazca slab at 21S revealed from accurate locations of intermediate-depth seismicity. In *American Geophysical Union, Fall Meeting 2006*. Abstract S43D–08.

Rondenay, S., Abers, G. A., & Van Keken, P. E. (2008). Seismic imaging of subduction zone metamorphism. *Geology*, *36*(4), 275–278. https://doi.org/10.1130/G24112A.1

Rosenbaum, G., & Mo, W. (2011). Tectonic and magmatic responses to the subduction of high bathymetric relief. *Gondwana Research*, *19*(3), 571–582. https://doi.org/10.1016/j.gr.2010.10.007

Ruegg, J. C., Campos, J., Armijo, R., Barrientos, S., Briole, P., Thiele, R., et al. (1996). The Mw = 8.1 Antofagasta (North Chile) Earthquake of July 30,1995: First results from teleseismic and geodetic data. *Geophysical Research Letters*, *23*(9), 917–920. https://doi.org/10.1029/96GL01026

Ruiz, S., Métois, M., Fuenzalida, A., Ruiz, J., Leyton, F., Grandin, R., et al. (2014). Intense foreshocks and a slow slip event preceded the 2014 Iquique Mw 8.1 earthquake. *Science*, *345*, 1165–1169. https://doi.org/10.1126/science.1256074

Rüpke, L. H., Morgan, J. P., Hort, M., & Connolly, J. A. D. (2004). Serpentine and the subduction zone water cycle. *Earth and Planetary Science Letters*, *223*(1–2), 17–34. https://doi.org/10.1016/j.epsl.2004.04.018

Saffer, D. M., & Tobin, H. J. (2011). Hydrogeology and mechanics of subduction zone forearcs: Fluid flow and pore pressure. *Annual Review of Earth and Planetary Sciences*, *39*(1), 157–186. https://doi.org/10.1146/annurev-earth-040610-133408

Scheuber, E., & Andriessen, P. A. M. (1990). The kinematic and geodynamic significance of the Atacama fault zone, northern Chile. *Journal of Structural Geology*, *12*(2), 243–257. https://doi.org/10.1016/0191-8141(90) 90008-M
Scholz, C. H. (1998). Earthquakes and friction laws. *Nature*, *391*, 37–42. https://doi.org/10.1038/34097
Scholz, C. H., & Campos, J. (2012). The seismic coupling of subduction zones revisited. *Journal of Geophysical Research*, *117*, B05310. https://doi.org/10.1029/2011JB009003
Schurr, B., Asch, G., Hainzl, S., Bedford, J., Hoechner, A., Palo, M., et al. (2014). Gradual unlocking of plate boundary controlled initiation of the 2014 Iquique earthquake. *Nature*, *512*(7514), 299–302. https://doi.org/10.1038/nature13681
Schurr, B., Asch, G., Rietbrock, A., Kind, R., Pardo, M., Heit, B., & Monfret, T. (1999). Seismicity and average velocities beneath the Argentine Puna plateau. *Geophysical Research Letters*, *26*(19), 3025–3028. https://doi.org/10.1029/1999GL005385
Schurr, B., Asch, G., Rosenau, M., Wang, R., Oncken, O., Barrientos, S., et al. (2012). The 2007 M7.7 Tocopilla northern Chile earthquake sequence: Implications for along-strike and downdip rupture segmentation and megathrust frictional behavior. *Journal of Geophysical Research*, *117*, B05305. https://doi.org/10.1029/2011JB009030
Schurr, B., Rietbrock, A., Asch, G., Kind, R., & Oncken, O. (2006). Evidence for lithospheric detachment in the central Andes from local earthquake tomography. *Tectonophysics*, *415*(1–4), 203–223. https://doi.org/10.1016/j.tecto.2005.12.007
Shillington, D. J., Becel, A., Nedimovic, M. R., Kuehn, H., Webb, S. C., Abers, G. A., et al. (2015). Link between plate fabric, hydration and subduction zone seismicity in Alaska. *Nature Geoscience*, *8*(12), 961–964. https://doi.org/10.1038/ngeo2586
Sippl, C., Schurr, B., Asch, G., & Kummerow, J. (2018). Catalogue of Earthquake Hypocenters for Northern Chile Compiled from IPOC (plus auxiliary) seismic stations. GFZ Data Services. https://doi.org/10.5880/GFZ.4.1.2018.001
Sippl, C., Schurr, B., Yuan, X., Mechie, J., Schneider, F. M., Gadoev, M., et al. (2013). Geometry of the Pamir-Hindu Kush intermediate-depth earthquake zone from local seismic data. *Journal of Geophysical Research: Solid Earth*, *118*, 1438–1457. https://doi.org/10.1002/jgrb.50128
Sodoudi, F., Yuan, X., Asch, G., & Kind, R. (2011). High-resolution image of the geometry and thickness of the subducting Nazca lithosphere beneath northern Chile. *Journal of Geophysical Research*, *116*, B04302. https://doi.org/10.1029/2010JB007829
Springer, M. (1999). Interpretation of heat-flow density in the Central Andes. *Tectonophysics*, *306*(3-4), 377–395. https://doi.org/10.1016/S0040-1951(99)00067-0
Storch, I., Buske, S., Schmelzbach, C., & Wigger, P. (2016). Seismic imaging of a megathrust splay fault in the North Chilean subduction zone (Central Andes). *Tectonophysics*, *689*, 157–166. https://doi.org/10.1016/j.tecto.2016.02.039
Syracuse, E. M., & Abers, G. A. (2006). Global compilation of variations in slab depth beneath arc volcanoes and implications. *Geochemistry, Geophysics, Geosystems*, *7*, Q05017. https://doi.org/10.1029/2005GC001045
Syracuse, E. M., Van Keken, P. E., Abers, G. A., Suetsugu, D., Bina, C., Inoue, T., et al. (2010). The global range of subduction zone thermal models. *Physics of the Earth and Planetary Interiors*, *183*(1–2), 73–90. https://doi.org/10.1016/j.pepi.2010.02.004
Tassara, A., Götze, H. J., Schmidt, S., & Hackney, R. (2006). Three-dimensional density model of the Nazca plate and the Andean continental margin. *Journal of Geophysical Research*, *111*, B09404. https://doi.org/10.1029/2005JB003976
Tatsumi, Y. (1986). Formation of the volcanic front in subduction zones. *Geophysical Research Letters*, *13*(8), 717–720. https://doi.org/10.1029/GL013i008p00717
Thurber, C. H. (1983). Earthquake locations and three-dimensional crustal structure in the Coyote Lake Area, Central California. *Journal of Geophysical Research*, *88*(B10), 8226–8236.
Trumbull, R., Ulrich, R., Oncken, O., Scheuber, E., Munier, K., & Hongn, F. (2006). The time-space distribution of Cenozoic volcanism in the south-central Andes: A new data compilation and some tectonic implications. In O. Oncken et al. (Eds.), *The Andes: Active subduction orogeny* (pp. 29–43). Berlin: Springer-Verlag.
Van Keken, P. E., Hacker, B. R., Syracuse, E. M., & Abers, G. A. (2011). Subduction factory: 4. Depth-dependent flux of H_2O from subducting slabs worldwide. *Journal of Geophysical Research*, *116*, B01401. https://doi.org/10.1029/2010JB007922
Victor, P., Sobiesiak, M., Glodny, J., Nielsen, S. N., & Oncken, O. (2011). Long-term persistence of subduction earthquake segment boundaries: Evidence from Mejillones Peninsula, northern Chile. *Journal of Geophysical Research*, *116*, B02402. https://doi.org/10.1029/2010JB007771
von Huene, R., & Scholl, D. W. (1991). Observations at convergent margins concerning sediment subduction, subduction erosion, and the growth of continental crust. *Reviews of Geophysics*, *29*(3), 279–316. https://doi.org/10.1029/91RG00969
Wada, I., & Wang, K. (2009). Common depth of slab-mantle decoupling: Reconciling diversity and uniformity of subduction zones. *Geochemistry, Geophysics, Geosystems*, *10*, Q10009. https://doi.org/10.1029/2009GC002570
Waldhauser, F., & Ellsworth, W. L. (2000). A double-difference earthquake location algorithm: Method and application to the Northern Hayward Fault, California. *Bulletin of the Seismological Society of America*, *90*(6), 1353–1368. https://doi.org/10.1785/0120000006
Wang, K. (2002). Unbending combined with dehydration embrittlement as a cause for double and triple seismic zones. *Geophysical Research Letters*, *29*, 1889. https://doi.org/10.1029/2002GL015441
Wang, K., & Bilek, S. L. (2014). Invited review paper: Fault creep caused by subduction of rough seafloor relief. *Tectonophysics*, *610*, 1–24. https://doi.org/10.1016/j.tecto.2013.11.024
Wigger, P., Salazar, P., Kummerow, J., Bloch, W., Asch, G., & Shapiro, S. A. (2016). West–fissure- and Atacama-fault seismic network (2005/2012) (Tech. rep.) Potsdam: Deutsches GeoForschungsZentrum GFZ. https://doi.org/10.14470/3S7550699980
Withers, M., Aster, R. C., Young, C., Beiriger, J., Harris, M., Moore, S., & Trujillo, J. (1998). A comparison of select trigger algorithms for automated global seismic phase and event detection. *Bulletin of the Seismological Society of America*, *88*(1), 95–106.
Wölbern, I., Heit, B., Yuan, X., Asch, G., Kind, R., Viramonte, J., et al. (2009). Receiver function images from the Moho and the slab beneath the Altiplano and Puna plateaus in the Central Andes. *Geophysical Journal International*, *177*(1), 296–308. https://doi.org/10.1111/j.1365-246X.2008.04075.x
Wörner, G., Moorbath, S., & Harmon, R. S. (1992). Andean Cenozoic volcanic centers reflect basement isotopic domains. *Geology*, *20*(12), 1103–1106. https://doi.org/10.1130/0091-7613(1992)020<1103:ACVCRB>2.3.CO;2
Yamasaki, T., & Seno, T. (2003). Double seismic zone and dehydration embrittlement of the subducting slab. *Journal of Geophysical Research*, *108*(B4), 2212. https://doi.org/10.1029/2002JB001918
Yano, T. E., Takeda, T., Matsubara, M., & Shiomi, K. (2017). Japan Unified hIgh-resolution relocated Catalog for Earthquakes (JUICE): Crustal seismicity beneath the Japanese Islands. *Tectonophysics*, *702*, 19–28. https://doi.org/10.1016/j.tecto.2017.02.017
Yoon, M., Buske, S., Shapiro, S. A., & Wigger, P. (2009). Reflection image spectroscopy across the Andean subduction zone. *Tectonophysics*, *472*(1–4), 51–61. https://doi.org/10.1016/j.tecto.2008.03.014
Yuan, X., Sobolev, S. V., Kind, R., Oncken, O., Bock, G., Asch, G., et al. (2000). Subduction and collision processes in the Central Andes constrained by converted seismic phases. *Nature*, *408*(6815), 958–961. https://doi.org/10.1038/35050073
Zhao, D., & Ohtani, E. (2009). Deep slab subduction and dehydration and their geodynamic consequences: Evidence from seismology and mineral physics. *Gondwana Research*, *16*(3–4), 401–413. https://doi.org/10.1016/j.gr.2009.01.005